AGU PUBLICATIONS

Journal of Advances in Modeling Earth Systems

RESEARCH ARTICLE

10.1002/2017MS001055

A Heuristic Parameterization for the Integrated Vertical Overlap of Cumulus and Stratus

Sungsu Park[1]

[1]School of Earth and Environmental Sciences, Seoul National University, Seoul, South Korea

Key Points:

- A heuristic parameterization was developed for the integrated vertical overlap of cumulus and stratus
- The parameterization was implemented into the Seoul National University Atmosphere Model version 0 and globally tested in an offline mode
- Compared with the dual cloud simulation, the simulation with a single-merged cloud substantially increases longwave cloud radiative forcing

Correspondence to:
S. Park,
sungsup@snu.ac.kr

Citation:
Park, S. (2017). A heuristic parameterization for the integrated vertical overlap of cumulus and stratus. *Journal of Advances in Modeling Earth Systems*, *9*, 2437–2465. https://doi.org/10.1002/2017MS001055

Received 21 MAY 2017
Accepted 2 OCT 2017
Accepted article online 4 OCT 2017
Published online 31 OCT 2017

Abstract The author developed a heuristic parameterization to handle the contrasting vertical overlap structures of cumulus and stratus in an integrated way. The parameterization assumes that cumulus is maximum-randomly overlapped with adjacent cumulus; stratus is maximum-randomly overlapped with adjacent stratus; and radiation and precipitation areas at each model interface are grouped into four categories, that is, convective, stratiform, mixed, and clear areas. For simplicity, thermodynamic scalars within individual portions of cloud, radiation, and precipitation areas are assumed to be internally homogeneous. The parameterization was implemented into the Seoul National University Atmosphere Model version 0 (SAM0) in an offline mode and tested over the globe. The offline control simulation reasonably reproduces the online surface precipitation flux and longwave cloud radiative forcing (LWCF). Although the cumulus fraction is much smaller than the stratus fraction, cumulus dominantly contributes to precipitation production in the tropics. For radiation, however, stratus is dominant. Compared with the maximum overlap, the random overlap of stratus produces stronger LWCF and, surprisingly, more precipitation flux due to less evaporation of convective precipitation. Compared with the maximum overlap, the random overlap of cumulus simulates stronger LWCF and weaker precipitation flux. Compared with the control simulation with separate cumulus and stratus, the simulation with a single-merged cloud substantially enhances the LWCF in the tropical deep convection and midlatitude storm track regions. The process-splitting treatment of convective and stratiform precipitation with an independent precipitation approximation (IPA) simulates weaker surface precipitation flux than the control simulation in the tropical region.

1. Introduction

General Circulation Models (GCMs) rely on the parameterizations to represent the impact of the subgrid variability of temperature and moisture. The partial cloudiness or cloud fraction between 0 and 1 (i.e., the fractional volume occupied by saturated air in each grid layer assuming vertical homogeneity within the individual grid layer) and associated subgrid fluctuation of cloud condensates are the byproducts of the subgrid variability parameterized by the Planetary Boundary Layer (PBL) and convection schemes, which are used in subsequent cloud microphysics and radiation schemes, and also aerosol wet deposition schemes in some GCMs. The vertical cloud overlap between adjacent model grid layers stems from the partial cloudiness, which is an inevitable aspect of any gridded numerical model with a finite vertical (Δz) and horizontal grid size $G \equiv \Delta x \Delta y$, where Δx, Δy, and Δz are the zonal, meridional, and vertical width of the model grid layer, respectively.

Numerous studies have been devoted to understanding the vertical cloud overlap through theoretical studies, observational analysis, and modeling. Geleyn and Hollingsworth (1979) hyphothesized that clouds in adjacent vertical grid layers are maximally overlapped (i.e., the overlap cloud fraction $a_{ovp} = \min[a(1), a(2)]$, where $a(1)$ and $a(2)$ are cloud fractions in the adjacent grid layers), while clouds separated by a cloud-free layer are randomly overlapped (i.e., $a_{ovp} = a(1) \cdot a(3)$). Extending this study, Hogan and Illingworth (2000, HI2000 hereinafter) found that the overlap of clouds at two levels rapidly decreases from the maximum to random overlap as their vertical separation increases. They proposed an inverse exponential expression for the degree of vertical cloud overlap as a function of the vertical separation distance. This hypothesis was tested with observational analysis using ground-based or satellite-derived observations and cloud-resolving models (e.g., Barker, 2008a, 2008b; Mace & Benson-Troth, 2002; Naud et al., 2008; Oreopoulos & Khairoutdinov, 2003; Oreopoulos & Norris, 2011; Tian & Curry, 1989; Willén et al., 2005). Modeling studies have shown that the parameterization of vertical cloud overlap has substantial impact on the simulated radiation (Barker et al., 1999, 2003; Collins, 2001; Li, 2000; Liang & Wang, 1997; Morcrette & Fouquart, 1986; Morcrette & Jakob, 2000; Stubenrauch et al., 1997), precipitation (Jakob & Klein, 1999, 2000; Liang & Wang, 1997; Morcrette & Jakob, 2000), and chemical species (Neu & Prather, 2012). Although different functional forms have also been suggested (e.g., Brooks et al., 2005; Neggers et al., 2011), the hypothesis suggested by HI2000 has served as a base framework for studying vertical cloud overlap.

The key parameter in the formulation of HI2000's hypothesis is the *e*-folding decorrelation length scale Δz_0. HI2000 showed that as the temporal and vertical resolutions of the analysis data become finer, Δz_0 tends to decrease and the vertical cloud overlap shifts from maximum to random. They also noted the dependence of Δz_0 on geographic locations and seasons. By analyzing ground-based cloud radar data, Mace and Benson-Troth (2002) found that the vertical cloud overlap in midlatitudes is a strong function of the season, suggesting the possibility of overlap parameterization in terms of cloud types. Based on the analysis of global satellite data, Barker (2008a) found that the global mean Δz_0 is about 2 (km), with a tendency for large values in the tropics and polar regions during winter. By analyzing ground-based radar and lidar data, Naud et al. (2008) determined a similar dependency of Δz_0 on the geographical location and seasons and speculated that the parameterization of Δz_0 as a function of environmental conditions, such as large-scale vertical motion, wind shear, or convective activity, might capture much of the important variability of vertical cloud overlap. Oreopoulos and Norris (2011) also showed that vertical cloud overlap has significant seasonal variations, with a tendency for more maximum overlap in summer months and in the larger domain size used to define the cloud fraction. In general, these observational studies indicate that Δz_0 should be defined for individual cloud types based on their own geographical and seasonal variations, instead of being defined for a single cloud constant.

The Community Atmosphere Model version 5 (CAM5; Park et al., 2014) includes two cloud types: cumulus and stratus. Cumulus is associated with nonlocal asymmetric turbulent eddies (i.e., convective plumes) parameterized by a convection scheme (Park & Bretherton, 2009), while stratus is associated with local symmetric turbulent eddies parameterized by a PBL scheme (Bretherton & Park, 2009) superposed on the grid mean state simulated by an advection scheme. Some models combine the convection and PBL schemes to represent subgrid variability and associated vertical transport (e.g., Siebesma et al., 2007) or include more cloud types (e.g., Lock et al., 2000). By extending CAM5, Park et al. (2017) diagnosed additional detrained cumulus that is generated from cumulus but is horizontally spread rather than vertically elongated. Because of its nonlocal nature, cumulus tends to be more maximal vertically overlapped than stratus. As the model grid size *G* decreases, the subgrid convective activity parameterized by the convection scheme becomes weaker, while the contribution of grid mean flow simulated by the advection scheme increases (Park, 2014a, 2014b). Most GCMs use primitive parameterizations for vertical cloud overlap. For example, CAM5 parameterizes the vertical overlap of a single-merged cloud instead of individual cloud types (i.e., cumulus and stratus are combined into a single cloud for use in the radiation scheme) and inconsistent vertical cloud overlap assumptions are employed in different physics parameterizations (Park et al., 2014).

As a first step toward the comprehensive and consistent treatment of vertical cloud overlap of individual cumulus and stratus in various physics parameterizations, the author derived a set of mathematical equations that computes the integrated vertical overlap structure of cumulus and stratus and associated radiation and precipitation areas in section 2. Subsequently, as described in section 3, the parameterization was implemented into the Seoul National University Atmosphere Model version 0 (SAM0) in an offline mode and tested over the globe for 1 year. Section 4 provides various simulation results including the sensitivity of grid mean radiation and precipitation fluxes to assumed vertical overlap of cumulus and stratus. The validity of two simplifying assumptions frequently used in GCMs, integration of cumulus and stratus in a single-merged cloud for radiation computation, and process-splitting treatment of convective and stratiform precipitations within separate convection and stratus microphysics schemes were examined. The summary and conclusion are provided in section 5.

2. Formulation

2.1. Basic Assumptions

It is assumed that each grid layer contains two types of clouds, cumulus and stratus, with the following geometries: (1) cumulus and stratus are horizontally nonoverlapped (but can be vertically overlapped

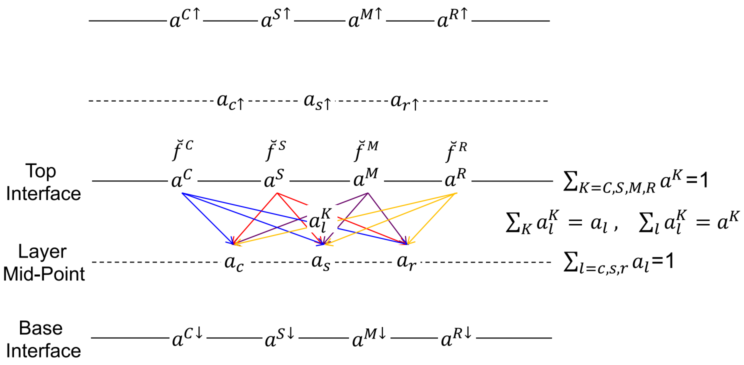

Figure 1. Diagram illustrating the vertical overlaps of cloud, radiation, and precipitation areas. The variable a_l at the layer midpoint is the cloud fraction with $l=c$ (cumulus), s (stratus), and r (clear portion); a^K at the model interface is the radiation or precipitation area with $K=C$ (convective), S (stratiform), M (mixed), and R (clear portion); $\breve{f}^K$ denotes the radiation or precipitation flux within individual radiation or precipitation area; and a_l^K is the overlap area between the radiation or precipitation area and the cloud fraction. Based on the consistency requirement, $\sum_K a^K=1$, $\sum_l a_l=1$, $\sum_K a_l^K=a_l$, and $\sum_l a_l^K=a^K$. The upward arrow denotes the value of the adjacent upper layer or upper interface, while the downward arrow marks the value at the base interface. Various cloud microphysics and radiation tendencies are computed within each portion of a_l^K, and subsequently summed up with the a_l^K weighting to compute the grid mean tendencies. The radiation or precipitation areas at the model interfaces are grouped into four categories, that is, convective, stratiform, mixed, and clear areas, based on the path history that the radiation or precipitation flux went through from the top (or the bottom for upward radiation) to the current model interface. Note that a^K and a_l^K of upward radiation differ from those of downward radiation and precipitation. For simplicity, the thermodynamic properties within individual portions of cloud, radiation, and precipitation areas are assumed to be internally homogeneous. See the text for more details.

between the grid layers), (2) cumulus is maximum-randomly overlapped with cumulus of the adjacent vertical layer, and (3) stratus is maximum-randomly overlapped with stratus of the adjacent vertical layer. Conceptually, because of the nonlocal nature of the associated turbulent eddies, cumulus is likely to be maximally overlapped with cumulus in vertical direction if no vertical shear exists in the mean horizontal wind. However, several observational studies showed that the vertical overlap of cumulus is not maximal at vertical grid-spacings smaller than the cumulus depth but tends to be random associated with small-scale irregularity, which has a greater influence than vertical wind shear and large-scale subsidence (Brooks et al., 2005; Corbetta et al., 2015; Neggers et al., 2011). To be compliant with these observational studies, our scheme was designed to handle both maximum and random cumulus overlap. The number of precipitation types is larger than the number of cloud types. For example, if convective precipitation falls into stratus that generates stratiform precipitation, the resulting precipitation type at the base of the stratus is mixed precipitation. Hereafter, including the clear-sky portion, it is assumed that there are three types of clouds at the layer midpoint (cumulus, stratus, and clear) and four types of precipitation at the model interface (convective, stratiform, mixed, and clear; see Figure 1). For simplicity, individual cloud and precipitation areas are assumed to be internally homogeneous.

In the following, the key variables and notations used in this paper are defined. For any variable ϕ, $\bar{\phi}$ will denote the mean value averaged over the grid box, $\breve{\phi}$ is the mean value averaged over an individual precipitation area at the model interface, and $\hat{\phi}$ is the mean value averaged over an individual cloud area at the layer midpoint. The variable a denotes the fractional area, where the subscripts c, s, and r stand for cumulus, stratus, and clear portion, respectively:

$$\sum_{l=1}^{3} a_l=1, \quad l=c,s,r, \tag{1}$$

the superscripts C, S, M, and R stand for convective, stratiform, mixed precipitation, and clear portion, respectively:

$$\sum_{K=1}^{4} a^K=1, \quad K=C,S,M,R, \tag{2}$$

and a_l^K denotes the overlapping area between a^K and a_l,

$$\sum_{l=1}^{3} a_l^K=a^K, \quad \sum_{K=1}^{4} a_l^K=a_l. \tag{3}$$

For a single cloud type, Jakob and Klein (2000) explored a similar approach of allocating the precipitation flux into a single type of homogeneous precipitation area in each layer. They showed that their approach reproduced most of the features of the more complex approach using multiple subcolumns in which the cloud fraction is either 0 or 1 (Jakob & Klein, 1999). Our approach can be understood as a generalization of Jakob and Klein (2000) for dual cloud types.

Similar to precipitation areas, four types of radiation areas can be defined. At the model interface, the convective (stratiform) radiation area is defined as the portion with radiation flux that has gone through cumulus (stratus) or cumulus and clear portions only. If radiation flux has gone through both cumulus and stratus, the corresponding portion is defined as mixed radiation area. If radiation flux has gone through the clear portion only, the corresponding portion is defined as clear radiation area. In contrast to the precipitation area, the radiation area is defined for each of downward and upward radiation fluxes. To avoid complexity in association with multiple scattering, only LW radiation is considered in this paper.

2.2. Vertical Overlap Between the Radiation or Precipitation Area and Cloud Area

In this section, the overlap area a_l^K between the radiation or precipitation area a^K at the top interface of an individual grid layer and the cloud area a_l at the layer midpoint is computed. The individual grid box is divided into N pixels and the number of possible ways to allocate $n^K = Na^K$ and $n_l = Na_l$ into N pixels is calculated. If i is the number of overlap pixels between a^K and a_l, the overlap area a_l^K is computed from the probability-weighted sum for all possible i values as follows:

$$a_l^K = \sum_{i=i_{\min}}^{i_{\max}} \left(\frac{i}{N}\right) \cdot \left\{\frac{W(i)}{W_{tot}}\right\}, \tag{4}$$

where W_{tot} is the total number of ways to allocate cumulus (Na_c), stratus (Na_s), and clear pixels (Na_r) into N pixels such that the assumed overlap assumption for cumulus and stratus is satisfied; $W(i)$ is the number of ways to allocate with i overlap pixels between Na^K and Na_l; i_{min} and i_{max} are the minimum and maximum number of overlap pixels between Na^K and Na_l; W_{tot} differs depending on whether stratus and cumulus are maximal or randomly overlapped; and $W(i)$ and (i_{min}, i_{max}) are the functions of individual radiation or precipitation and cloud types being considered. Appendix A provides a detailed explanation of the computation of the 12 overlap areas of a_l^K for each combination of cumulus and stratus overlaps—$a_l^K|^{\max,c}_{\max,s}$ for maximum cumulus and maximum stratus overlaps, $a_l^K|^{\max,c}_{ran,s}$ for maximum cumulus and random stratus overlaps, $a_l^K|^{ran,c}_{\max,s}$ for random cumulus and maximum stratus overlaps, and $a_l^K|^{ran,c}_{ran,s}$ for random cumulus and random stratus overlaps—for each combination of $K = C, S, M, R$ and $l = c, s, r$. The final a_l^K is obtained by

$$a_l^K = \lambda_c \cdot [\lambda_s \cdot a_l^K|^{\max,c}_{\max,s} + (1-\lambda_s) \cdot a_l^K|^{\max,c}_{ran,s}] + (1-\lambda_c) \cdot [\lambda_s \cdot a_l^K|^{ran,c}_{\max,s} + (1-\lambda_s) \cdot a_l^K|^{ran,c}_{ran,s}], \tag{5}$$

and following HI2000, the weighting factors for cumulus (λ_c) and stratus (λ_s) overlap are parameterized as

$$\lambda_c = \exp(-\Delta z/\Delta z_c), \quad \lambda_s = \exp(-\Delta z/\Delta z_s), \tag{6}$$

where Δz is the vertical separation distance between two adjacent grid layers and Δz_c and Δz_s are the constant decorrelation length scales for cumulus and stratus, respectively. For the default control simulation, Δz_c is set to ∞ (i.e., maximum cumulus overlap) and Δz_s is set to 2 (km) following the previous observational analysis (e.g., HI2000; Barker, 2008a). If $\Delta z = 0$, $\lambda_c = \lambda_s = 1$ and $a_l^K = a_l^K|^{\max,c}_{\max,s}$, but if $\Delta z \to \infty$, $\lambda_c = \lambda_s = 0$ and $a_l^K = a_l^K|^{ran,c}_{ran,s}$. If $\Delta z_c = 0$, $a_l^K = \lambda_s \cdot a_l^K|^{ran,c}_{\max,s} + (1-\lambda_s) \cdot a_l^K|^{ran,c}_{ran,s}$, while if $\Delta z_c = \infty$, $a_l^K = \lambda_s \cdot a_l^K|^{\max,c}_{\max,s} + (1-\lambda_s) \cdot a_l^K|^{\max,c}_{ran,s}$.

Using a_l^K, the radiation areas at the base interface $a^{K\downarrow}$, grid mean production rates of radiation $\bar{H}_l$, and the grid mean radiation flux at the base interface $\bar{f}^{K\downarrow}$ can be computed, as described in Appendix B (see Figure 1). Similar computations for the grid mean precipitation production rate $\bar{P}_l$ and the evaporation rate of precipitation $\bar{E}_r$ are explained in Appendix C. Although common notations are used, it should be noted that the numerical values of a_l^K for radiation differ from those of a_l^K for precipitation when no precipitation is generated within the cloud or when the precipitation completely evaporates in the clear sky.

3. Simulation Setting

Community Atmosphere Model version 5 (CAM5; Park et al., 2014) combined with a Unified Convection Scheme (UNICON; Park, 2014a, 2014b) with a revised treatment of convective detrainment processes (Park et al., 2017) was used as a host model to test the overlap parameterization. Hereafter, this host model will be referred to as the Seoul National University Atmosphere Model version 0 (SAM0). A description of SAM0 and its global performance is provided in Park et al. (2017).

The vertical profiles of the fractional area and in-cloud condensate mass of cumulus and stratus at each time step in each grid column are fed into the vertical cloud overlap equations to compute a_l^K, a^K, $\bar{P}_l$, $\bar{E}_r$, $\bar{H}_l$, and $\bar{f}^K$ for each precipitation and radiation field. To assess the isolated impact of vertical cloud overlap without the feedback on other physics and dynamic processes, the overlap parameterization was implemented into SAM0 in an offline mode such that it does not interfere with the internal model integration. The offline simulation computes the production and evaporation rates of precipitation and radiative heating using the equation described in Appendix D, that is, a simplified version of the more complex ones used in the online SAM0. To mimic the online simulation, the offline simulation neglects both the homogeneous and heterogeneous accretion processes within cumulus. After a series of tuning exercises to mimic the online simulation results, the values of tunable parameters for offline control simulation were determined, as described in Appendix D. Based on these configurations, a global standalone simulation was conducted, forced by the observed climatological sea surface temperature (SST) and sea-ice fraction with an annual cycle for 1 year at a horizontal resolution of 0.9° latitude × 1.25° longitude with 30 vertical layers and a model integration time step of $\Delta t = 30$ min, as described in Park et al. (2014). As shown later in this article, our offline control simulation reproduces the online simulation well.

4. Results

4.1. Control Simulation

4.1.1. Precipitation Flux at the SFC and LWCF at the TOA

Figure 2 shows the annual mean precipitation flux at the surface (SFC) and the LWCF at the top of the atmosphere (TOA). Both the offline control and online SAM0 simulations overestimate the observed global mean surface precipitation rate but underestimate LWCF at the TOA. As noted by Park et al. (2014), some of the former biases might be associated with low biases in the satellite-estimated precipitation (Stephens et al., 2012) and some of the latter biases are due to the use of grid mean water vapor instead of clear-sky water vapor in computing clear-sky radiation in the simulations. In the midlatitude storm track, SAM0 systematically overestimates the observed surface precipitation rate (Figure 2d); the simulated liquid water path (LWP) is substantially smaller than the observation (not shown). It is speculated that incomplete model physics (e.g., the stratiform microphysics scheme) and errors of the satellite-estimated precipitation contributes to these precipitation biases.

The control simulation reproduces the SAM0 simulation well, although the two simulations use different stratus microphysics, radiation, and vertical cloud overlap schemes. As described in Appendix D, the stratus microphysics used for the control simulation consist of single-moment autoconversion and accretion processes of cloud liquid condensate only, neglecting other complex conversion processes involving phase changes employed in SAM0. The unified convection scheme in SAM0 explicitly computes the vertical variations of the radius and the center coordinate of cumulus updraft plume as a function of the vertical wind shear without assuming maximum cumulus. Both SAM0 and the control simulation, however, assume that cumulus generates convective precipitation only when the in-cumulus condensate is larger than 0.6 (g kg^{-1}). Instead of the maximum-random stratus overlap used in the control simulation, SAM0 employees the bulk maximum-random overlap of a single-merged cloud fraction in the radiation scheme and a simplified maximum stratus overlap in the stratus microphysics scheme that neglects the decrease of the precipitation area when stratiform precipitation completely evaporates in the clear sky. It is speculated that the similarity of the two simulation results is mainly due to the use of an identical cloud fraction and in-cloud condensate amount at every time step, rather than indicating the insensitivity of the simulated precipitation and radiation fields to the detailed treatment of cloud microphysics, radiation, and vertical cloud overlap processes. If our vertical cloud overlap scheme is implemented in an online mode, allowing interactive feedback with other physics and dynamics processes, the difference between the two simulations will likely be amplified. The following section will describe how the vertical cloud overlap contributes to detailed radiation and precipitation processes of the control simulation.

4.1.2. Zonal Mean Cloud and Precipitation Areas

Figures 3 and 4 show the zonal mean cross sections of annual mean cloud and precipitation areas, respectively, obtained from the offline control simulation. In our model, cumulus fraction (a_c) is defined as the saturated updraft fractional area of subgrid nonlocal asymmetric turbulent eddies, that is, the ratio of the mass flux and vertical velocity of convective updraft plumes in the unified convection scheme (Park, 2014a). The stratus fraction (a_s) is defined as the sum of two cloud elements: one is the saturated fractional area of subgrid local symmetric turbulent eddies, which is parameterized as a function of the environmental relative humidity and in-cloud ice condensate amount (Park et al., 2014); and the other is the detrained cumulus fraction that is parameterized as a function of the amount of detrained convective condensates and environmental relative humidity (Park et al., 2017). The computation of the precipitation areas shown in Figure

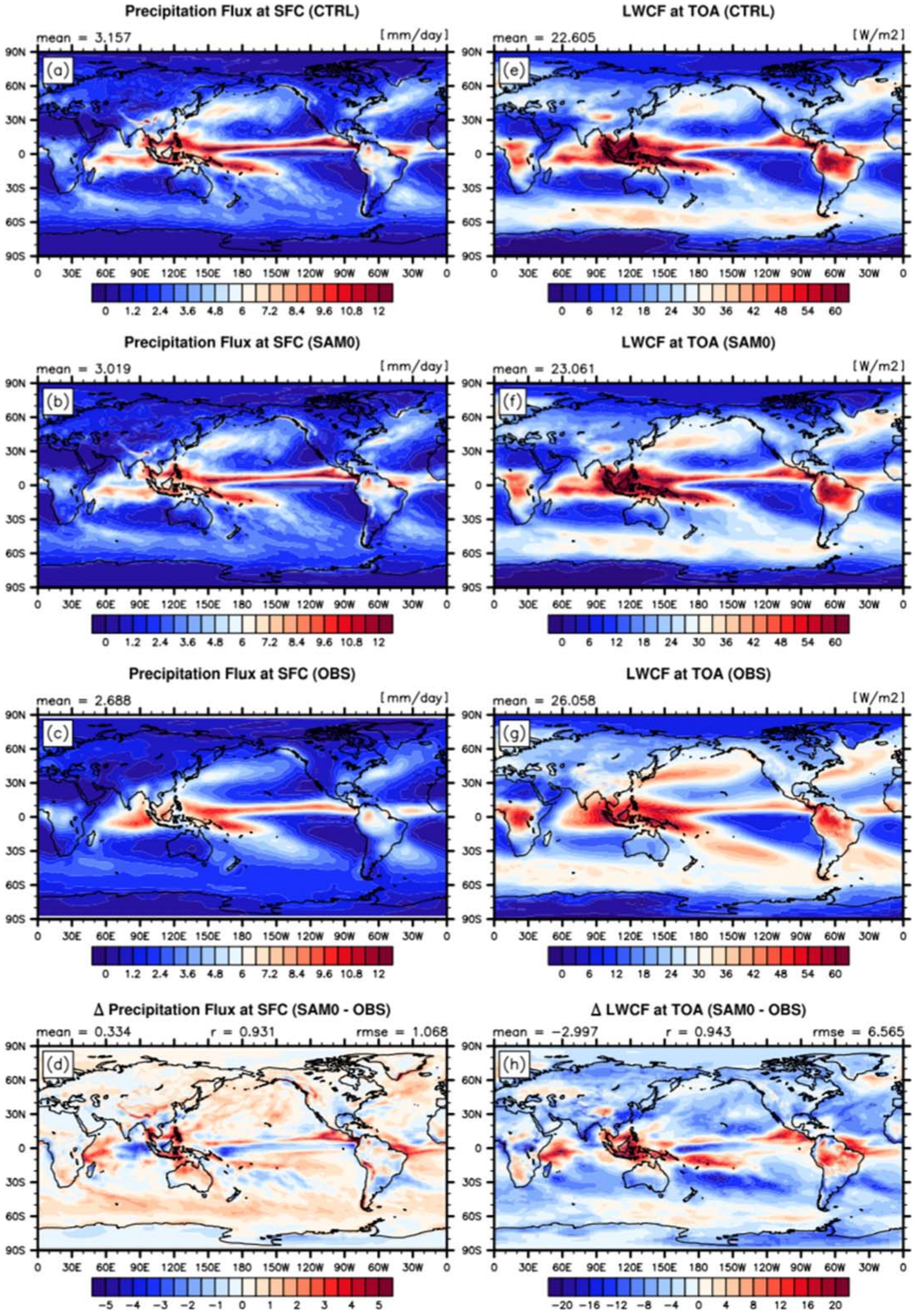

Figure 2. Annual mean (left) precipitation flux at the SFC and (right) LWCF at the TOA from (a, e) the offline control simulation (CTRL), (b, f) the online SAM0 simulation (SAM0), and (c, g) observations (OBS). The observations are the 20 year climatology of the surface precipitation rate from CMAP (January 1979 to December 1998; Xie & Arkin, 1996) and the 10 year climatology of LWCF from CERES-EBAF (March 2000 to February 2010; Loeb et al., 2009). The biases of the SAM0-simulated precipitation flux at the SFC and LWCF at the TOA compared with that of the OBS are shown in (d) and (h), respectively. The area-weighted global mean value is denoted as *mean* in the top left of individual plots corresponding with unit and color scales in the top right and bottom of each plot, respectively. In (bottom), *r* and *rmse* at the top of each plot denote the global pattern correlation and the root-mean-square error between SAM0 and OBS, respectively. Similar plotting rules were used for the following plots.

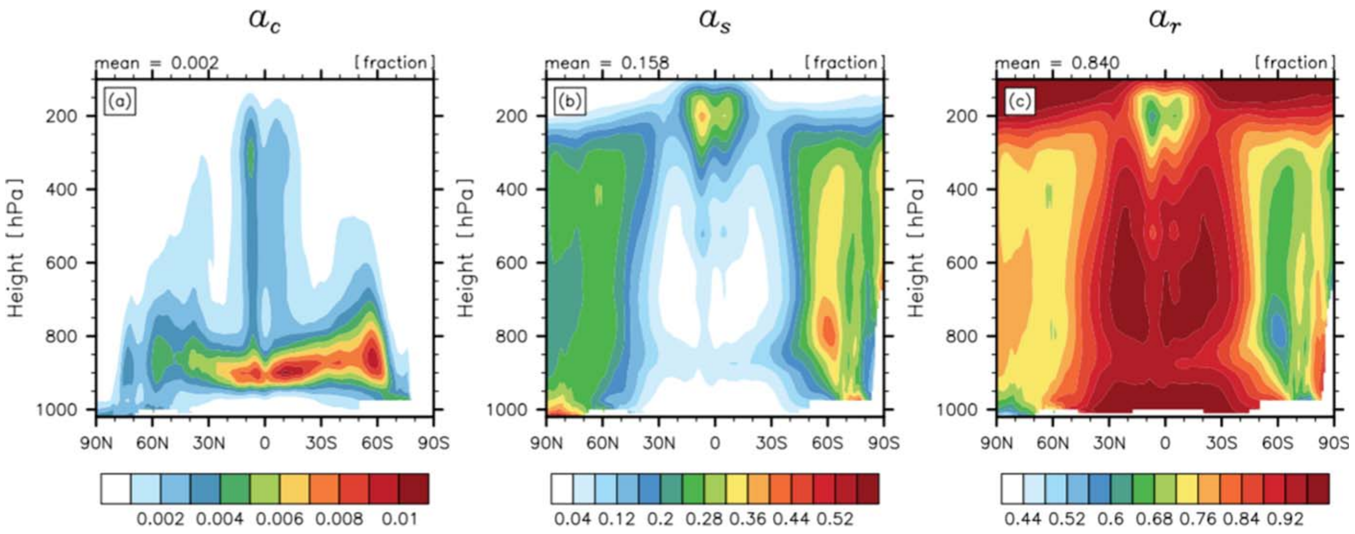

Figure 3. Annual zonal mean (a) cumulus fraction (a_c), (b) stratus fraction (a_s), and (c) clear fraction (a_r). In each grid layer, $\sum_l a_l = 1$. The global mean value weighted by the pressure thickness is denoted as *mean* in the top left of the individual plots; similar plotting rules were applied to the following cross-sectional plots.

4 requires additional assumptions with respect to vertical cloud overlap and cloud microphysical processes. If clouds are maximally overlapped in vertical direction and all clouds generate precipitation that not completely evaporates in the clear sky, the precipitation area at any model interface is identical to the maximum cloud fraction of the layers above the current model interface. In fact, this is the way how the stratus microphysics scheme of SAM0 computes the stratiform precipitation area. However, in reality, stratus is not maximally overlapped in vertical direction and weak stratiform precipitation can completely evaporate in the clear sky. In contrast to SAM0, our offline control simulation assumes that stratus is maximum-randomly overlapped in vertical direction and weak precipitation can completely evaporate in the clear sky; therefore, the precipitation area can decrease as the precipitation falls. The precipitation areas shown in Figure 4 show a third category of precipitation, that is, mixed precipitation (a^M), which characterizes the degree of vertical overlap between precipitating cumulus and stratus.

The cumulus fraction (a_c) is one or two orders smaller than the stratus fraction (a_s). The clear-sky fraction (a_r) is generally larger than a_s and a_c, except in the Arctic near the surface, where $a_s > 0.5$, a_c is a local maximum, and a_r has the minimum value. Deep cumulus above 200 hPa solely exists in the tropical region; however, moderate cumulus above 500 hPa also exists in midlatitude storm tracks in both hemispheres. In the tropical region, a_c is close to zero below 950 hPa, indicating that convective updraft initiated at the surface is in a nonsaturated dry state within PBL, with a lifting condensation level (LCL) of around 950 hPa. On the other hand, some convective updrafts in the Arctic and in midlatitude storm track regions at 60°N and 65°S are produced in a saturated state at the surface. The cumulus fraction is maximal in the layers between 900 and 850 hPa, with the largest value at 58°S. Stratus is abundant in the tropical upper troposphere, midlatitude storm tracks throughout the deep troposphere, and in polar regions. It is likely that the maximum a_s in the tropical upper troposphere is caused by detrained convective condensates, while the maximum a_s in midlatitude storm tracks is associated with strong grid mean upward motion.

Similar to clouds, a^S is much larger than a^C, which is slightly smaller than a^M. In contrast to clouds, precipitation areas tend to decrease with height; however, a^S shows the opposite variation in the mid and upper tropical troposphere, implying that stratiform precipitation in this region has a weak in-precipitation flux such that some of the stratiform precipitation completely evaporates in the clear sky. Furthermore, a^C is maximum within PBL in tropical regions, while a^S is large in midlatitude and polar regions near the surface, with a maximum value at 60°S, where a^R has the lowest value; a^M shows maximum values in tropical regions and in the midlatitude lower troposphere in which the product of a^C and a^S seems to be maximal. The observed a^R value can be used to evaluate the parameterized vertical cloud overlap and cloud microphysical processes in an integrated way.

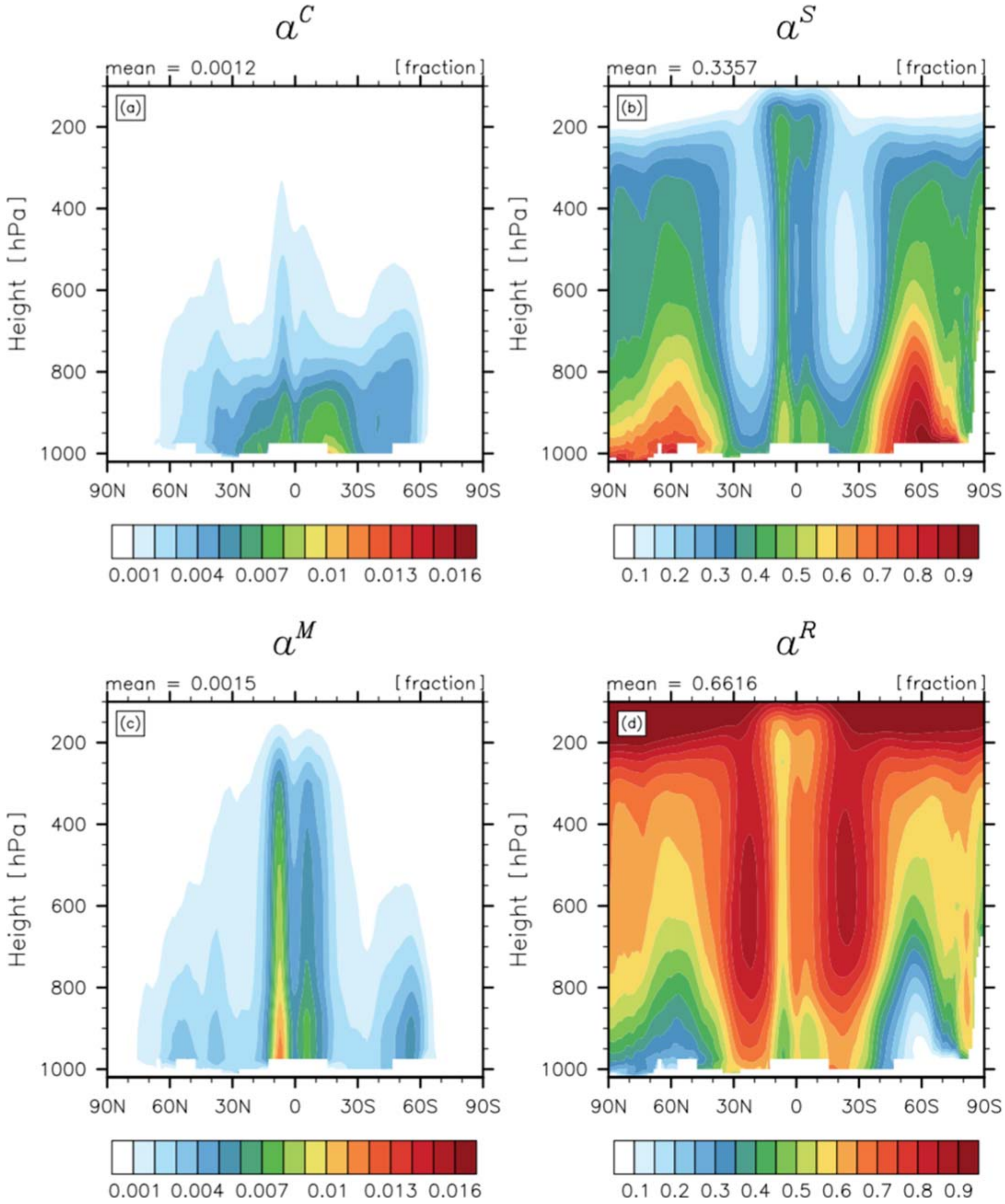

Figure 4. Annual zonal mean (a) convective precipitation area (a^C), (b) stratiform precipitation area (a^S), (c) mixed precipitation area (a^M), and (d) clear area (a^R). At each model interface, $\sum_K a^K=1$.

4.1.3. Overlap Areas Between Precipitation and Cloud Areas

Figure 5 shows the zonal mean cross sections of annual mean overlap areas between the precipitation areas at the top interface of individual grid layers and the cloud areas at the layer midpoint. Note that $a_c^K+a_s^K+a_r^K=a^K$ for each $K=C,S,M,R$; both autoconversion and accretion can occur in a_c^C, a_s^C, a_c^S, a_s^S, a_c^M, and a_s^M; autoconversion occurs in a_c^R and a_s^R; and evaporation of precipitation occurs in a_r^C, a_r^S, and a_r^M. Typical operational GCMs with a process-splitting treatment of convective and stratiform precipitation using independent precipitation approximation (IPA; Park, 2014a) neglects heterogeneous accretion within a_s^C and a_c^S such that mixed precipitation is not generated and $a_c^M=a_s^M=a_r^M=0$.

Because of the maximum cumulus overlap, the convective precipitation above the cumulus base mainly falls into cumulus (a_c^C). However, some of the convective precipitation above the cumulus base also falls

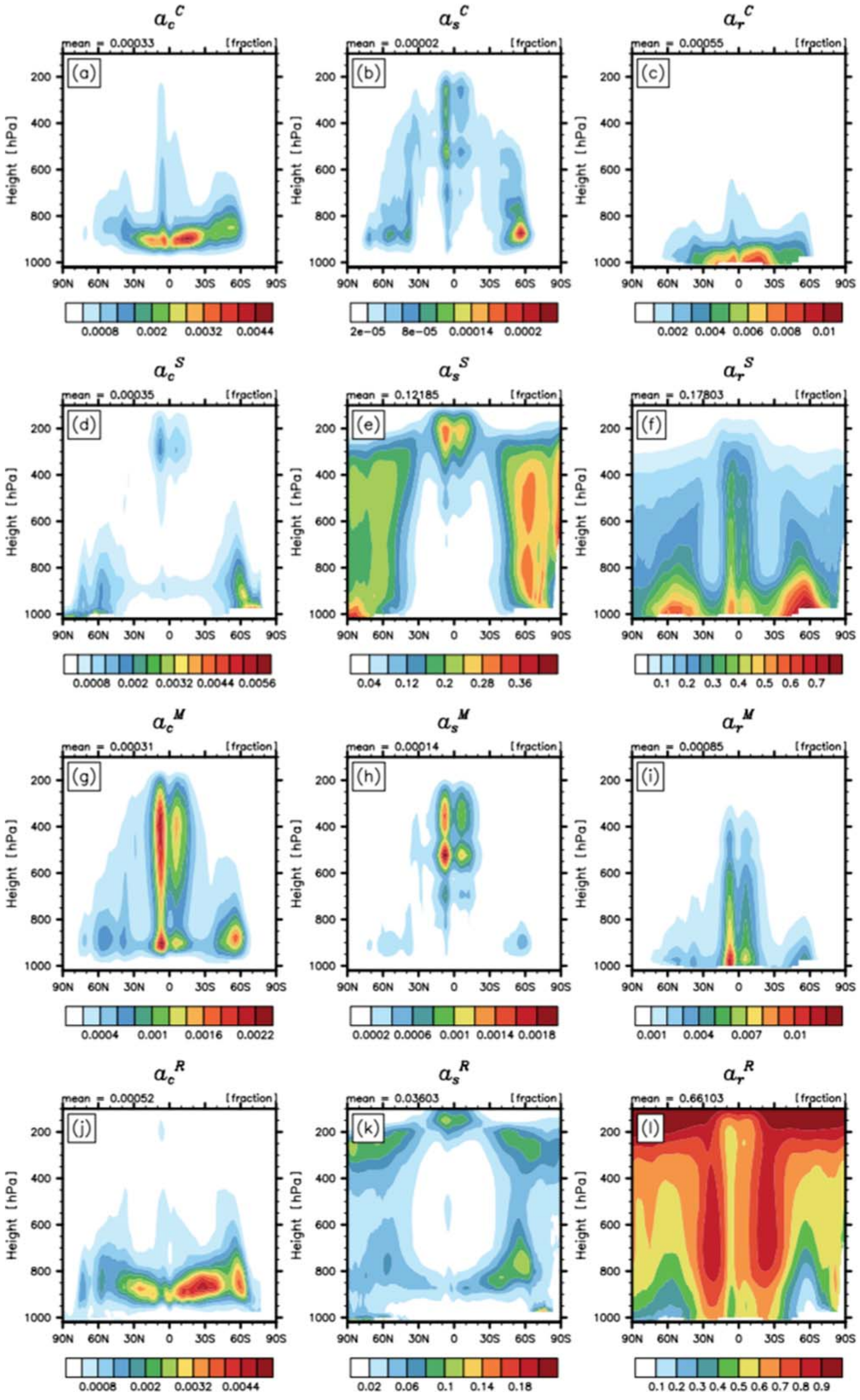

Figure 5. Annual zonal mean overlap areas (a_l^K) between the precipitation area at the top interface of individual grid layers (a^K) and the cloud area at the layer midpoint (a_l) for each combination of $K=C, S, M, R$ and $l=c, s, r$. In each grid layer, $\sum_l a_l^K = a^K$ and $\sum_K a_l^K = a_l$.

into the clear sky (a_r^C) in which convective precipitation evaporates and, to a much smaller extent, into the stratus (a_s^C) in which mixed precipitation is generated by heterogeneous accretion. Our cloud overlap scheme assumes that $a^C - a_c^C$ at the top interface of the individual grid layers randomly overlaps with $1 - a_c^C$ at the layer midpoint. Thus, the existence of nonzero $a_r^C + a_s^C$ above the cumulus base implies that the cumulus fraction increases with height in some grid columns. Below the cumulus base, most convective precipitation falls into the clear sky, as expected. In accordance with precipitation areas, evaporation areas (a_r^C, a_r^S, a_r^M) generally decrease with height, showing maximum values near the surface.

The fractional area in which homogeneous accretion of cumulus condensates can occur is large in the tropical and midlatitude lower troposphere (Figure 5a), while homogeneous accretion of stratus condensates mainly occurs in the tropical upper troposphere and deep troposphere in midlatitude and polar regions (Figure 5e). The areas in which mixed precipitation is initiated through heterogeneous accretion are much smaller than the areas in which homogeneous accretion can occur ($a_s^C \ll a_c^C$, $a_c^S \ll a_s^S$), implying that the process-splitting treatment of convective and stratiform precipitations with IPA in typical GCMs is justified. Although the magnitude of a_c^C is roughly similar to that of a_c^S, the precipitation production within a_c^C is larger than that within a_c^S (not shown) because the convective precipitation flux within a^C is stronger than the stratiform precipitation flux within a^S. In principle, mixed precipitation is generated within a_s^C and a_c^S; however, to mimic the online treatment of precipitation processes within SAM0, any accretion processes within a_c were neglected. As a result, unless cumulus generates convective precipitation through autoconversion, stratiform precipitation passing through a_c^S will still be identified as stratiform precipitation at the base interface. This explains why a^M in Figure 4c is zero over the Arctic area near the surface, although a_c^S is the local maximum. Note the similar patterns of a_s^C, a_c^M, and a_s^M. The overall magnitude of a_r^M is much smaller than that of a_r^S but is larger than a_r^C.

Pure autoconversion without accretion occurs within a_c^R and a_s^R. The pattern of a_c^R is similar to that of a_c, except in the tropical mid and upper troposphere in which various types of precipitations fall into the cumulus (a_c^C, a_c^S, a_c^M). The current UNICON diagnostically raises convective updraft plumes from the surface to the cumulus top only one time at each time step, without any vertical iteration loop. Thus, SAM0 does not treat homogeneous accretion of cumulus condensate by convective precipitation, neither does the offline control simulation. To reproduce the observed amount of the global mean precipitation rate at the surface in this situation, the autoconversion of cumulus condensate needs to be unrealistically large. One of the future research subjects is to implement the online accretion process within cumulus and to reduce corresponding model biases. Pure autoconversion of stratus condensate without accretion occurs in the upper and lower troposphere (Figure 5k). The clearest regions with minimal cloud and precipitation areas in the troposphere exist at 25°N/S, where the Hadley circulation subsides, while the gloomiest regions exist at 60°S and in the Arctic near the surface (Figure 5l).

4.1.4. Zonal Mean Precipitation Processes

Figure 6 shows the zonal mean cross sections of annual grid mean production rates of precipitation within cumulus (Figure 6a, $\bar{P}_c$) and stratus (Figure 6b, $\bar{P}_s$), and the grid mean evaporation rate of precipitation within clear sky (Figure 6c, $\bar{E}_r$). The grid mean production rate of precipitation is the sum of the product of in-cloud production rates of precipitation and the corresponding overlap areas shown in Figure 5. The grid mean evaporation rate of precipitation is computed in a similar way. In the tropical region, most of the precipitation is produced by cumulus, while it is generated by stratus in the midlatitude and tropical upper troposphere. In the tropical mid and upper troposphere, the precipitation production pattern is roughly similar to that of the corresponding cloud fraction; however, they are slightly offset in midlatitude regions. The grid mean evaporation rate of precipitation is large in the tropical region, with the maximum value near the surface at which a_r is also maximal. The global mean evaporation rate of precipitation is approximately one tenth of the global mean production rate of precipitation. The global mean cumulus fraction is much smaller than the stratus fraction; however, the grid mean precipitation production within the cumulus is as large as that within stratus, implying that the in-cumulus production rate of precipitation is much larger than that within stratus.

Figure 7 shows the zonal mean cross sections of annual grid mean precipitation fluxes. Most convective precipitation fluxes are concentrated in the tropical region, while strong stratiform precipitation fluxes exist in midlatitude regions. In the tropics, the mixed precipitation flux is stronger than the convective precipitation flux. The total precipitation flux shows dual maxima (Figure 7d), that is, one in the tropics and the other in

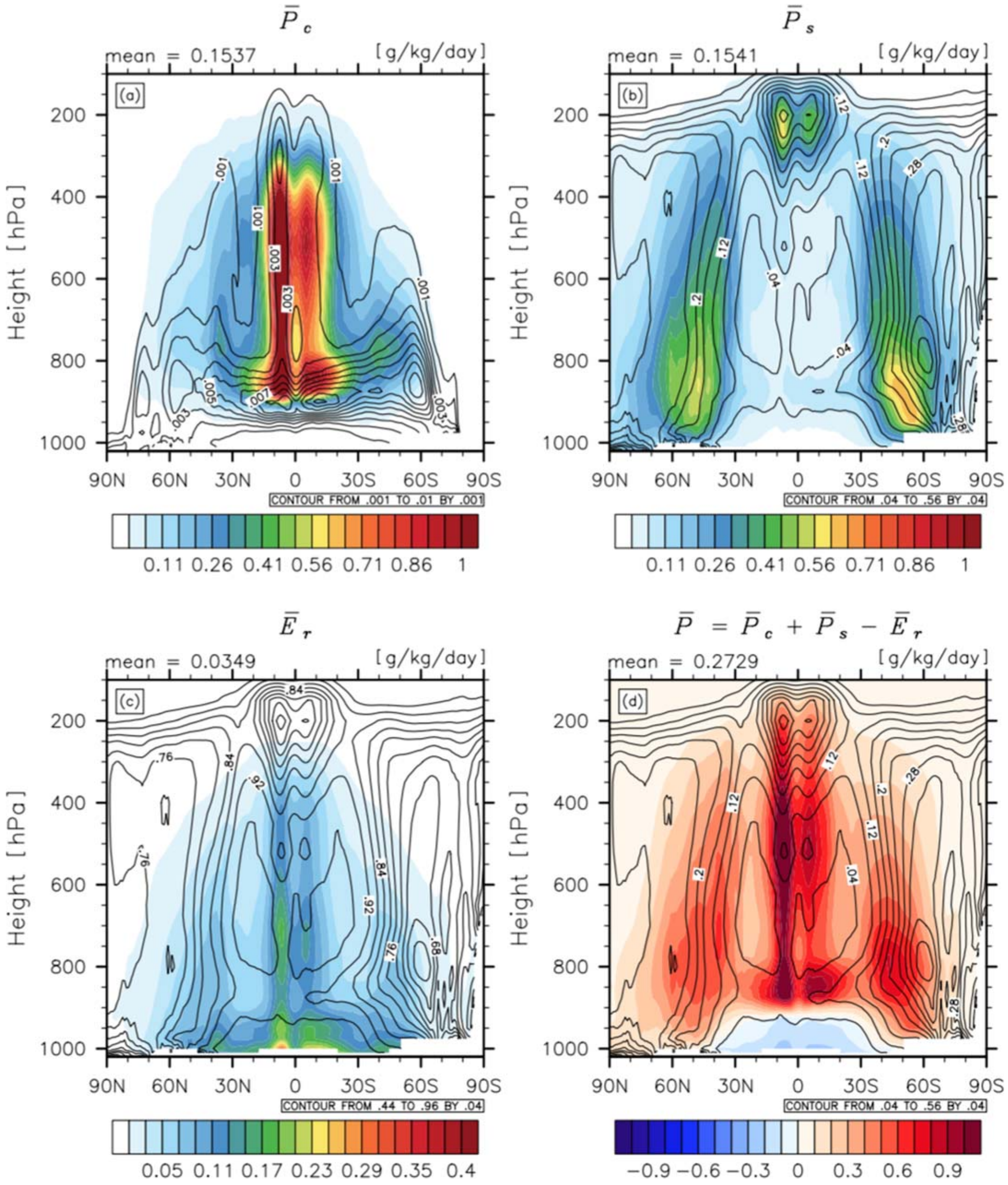

Figure 6. Annual zonal mean, grid mean (a) production rate of precipitation within cumulus ($\bar{P}_c$), (b) production rate of precipitation within stratus ($\bar{P}_s$), (c) evaporation rate of precipitation within clear sky ($\bar{E}_r$), and (d) total production rate of precipitation ($\bar{P}=\bar{P}_c+\bar{P}_s-\bar{E}_r$). The solid lines in each plot are (a) a_c, (b) a_s, (c) a_r, and (d) a_c+a_s.

midlatitude regions at 45°N/S, with a local minimum at 25°N/S, where downwelling branches of the Hadley circulation exist. The precipitation flux of all precipitation components tends to decrease with the height.

4.1.5. Zonal Mean Radiation Processes

Figure 8 shows the zonal mean cross sections of the annual grid mean LW heating rates of cumulus, stratus, clear-sky, all-sky, and cloud condensates for upward, downward, and net upward radiation fluxes. The LW heating rate of cloud condensates is computed by subtracting the cloud-free radiative heating rate obtained from running the radiation scheme with zero in-cloud condensates from all-sky LW heating rates. Figure 9 shows the resulting grid mean upward, downward, and net upward LW fluxes and LWCF, which is obtained by subtracting the cloud-free net upward LW flux from the all-sky net upward LW flux at each level.

In general, both the cloud and clear sky are heated by absorbing upward LW radiation, while being cooled by emitting downward LW radiation. Cancellation occurs between the heating and cooling; however,

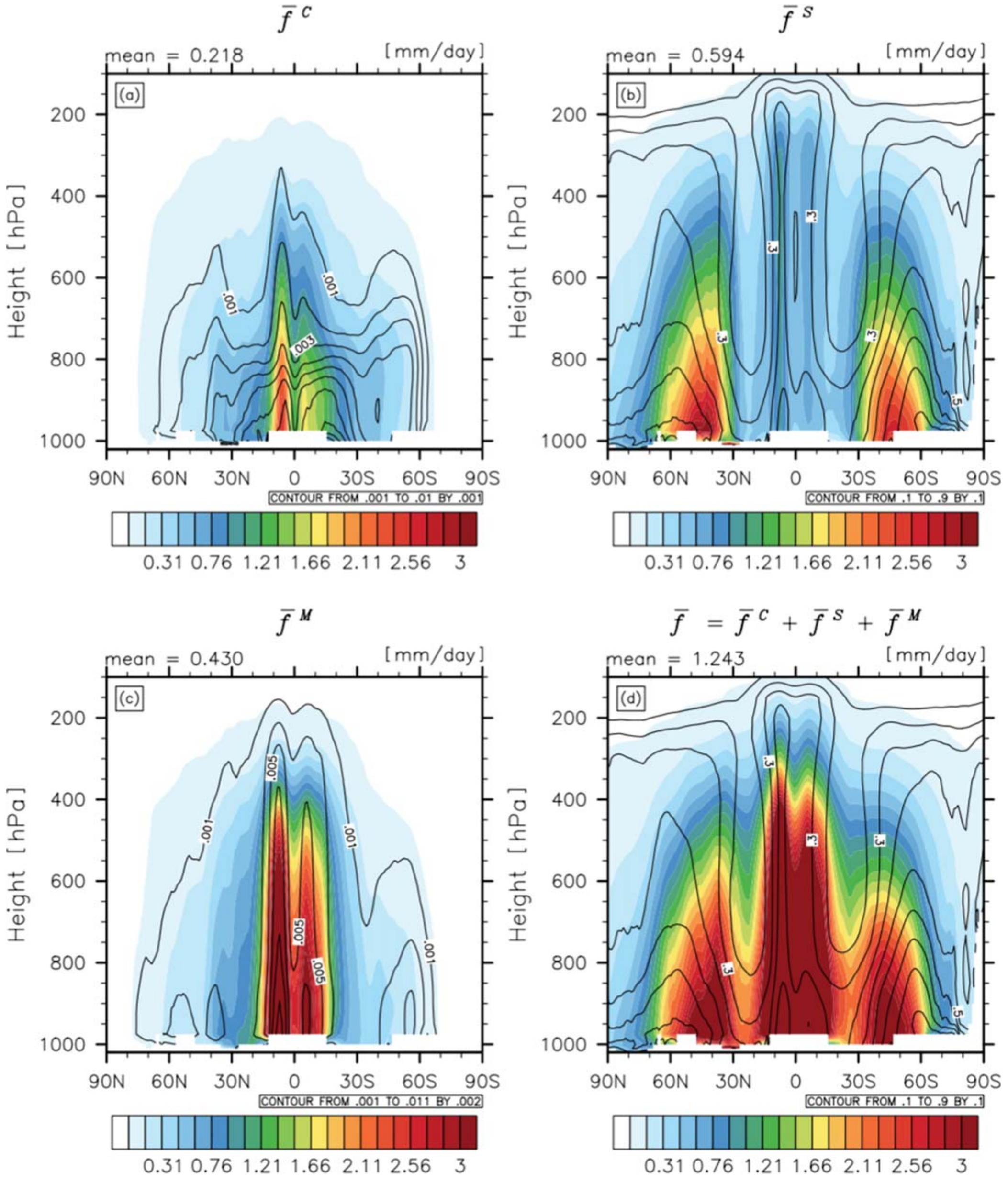

Figure 7. Annual zonal mean, grid mean (a) convective precipitation flux ($\bar{f}^C$), (b) stratiform precipitation flux ($\bar{f}^S$), (c) mixed precipitation flux ($\bar{f}^M$), and (d) total precipitation flux ($\bar{f}=\bar{f}^C+\bar{f}^S+\bar{f}^M$). The solid lines in each plot are (a) a^C, (b) a^S, (c) a^M, and (d) $a^C+a^S+a^M$.

cooling prevails. In contrast to precipitation production, cumulus-induced LW cooling is much weaker than stratus-induced LW cooling. The global mean net LW cooling induced by cumulus and stratus is approximately one third of that of clear sky. In the clear sky, upward LW heating is maximal in the tropical PBL, while downward LW cooling is maximal in the subtropical lower troposphere. The upward LW heating in the clear sky is slightly negative in the polar lower troposphere, where temperature inversion exists during boreal winter. The all-sky net LW heating rate is strongly negative in the mid and lower troposphere, mainly due to the cooling by water vapor (Figure 8l). The LW heating induced by cloud condensates (fifth row of Figure 8) resembles the sum of LW heating rates induced by cumulus (first row) and stratus (second row) but are slightly different. Upward LW heating induced by cloud condensate is maximal in the tropical upper troposphere and, to a smaller degree, in the midlatitude lower troposphere (Figure 8m), which are offset by the downward LW component that cools the atmosphere in and slightly above the clouds but warms the

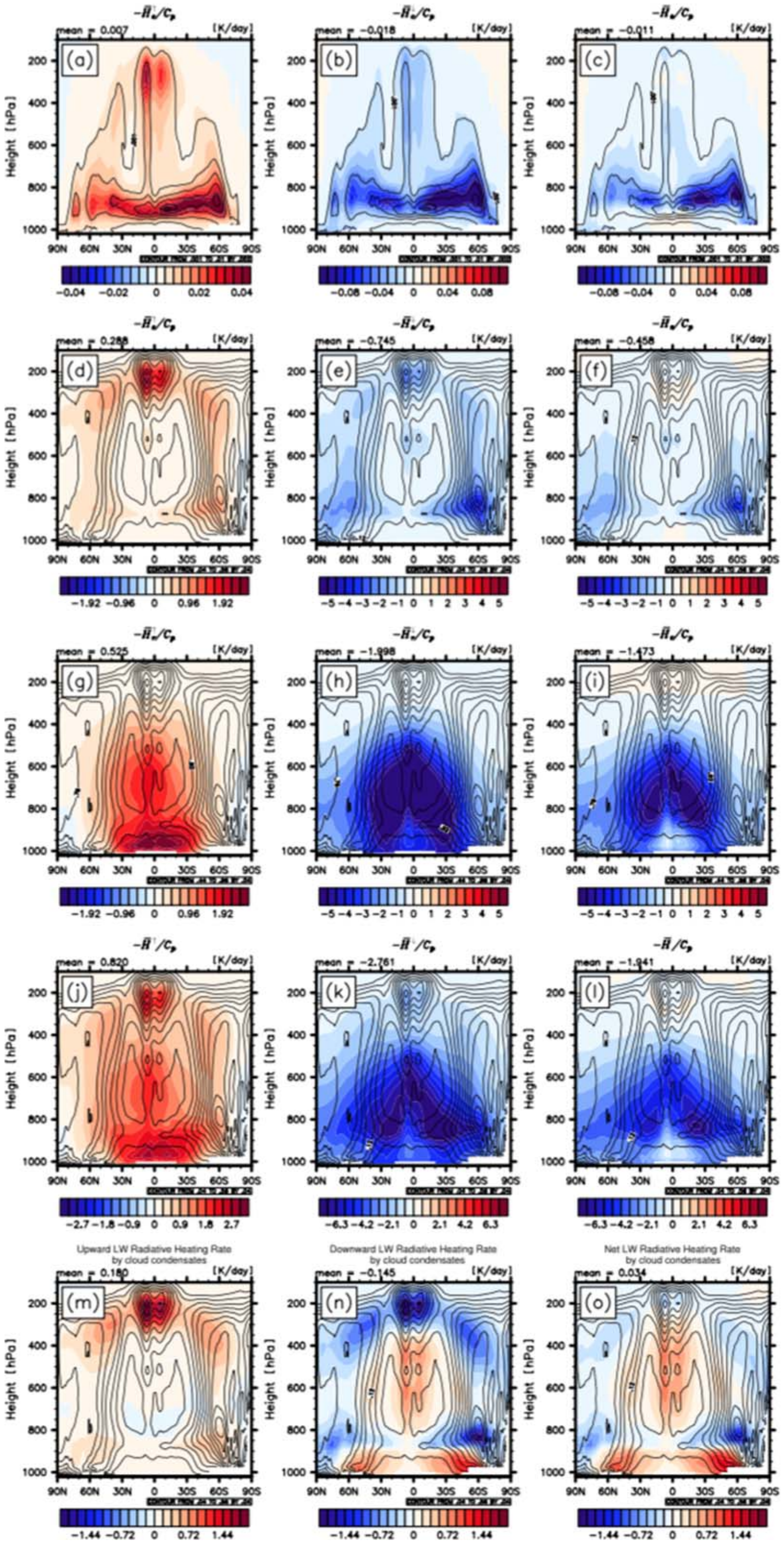

Figure 8. Annual zonal mean, grid mean LW heating rates of (first row) cumulus ($-\bar{H}_c/C_p$), (second row) stratus ($-\bar{H}_s/C_p$), (third row) clear-sky ($-\bar{H}_r/C_p$), (fourth row) all-sky ($-\bar{H}/C_p=-(\bar{H}_c+\bar{H}_s+\bar{H}_r)/C_p$), and (fifth row) cloud condensates for (left) upward, (middle) downward, and (right) net upward (i.e., upward – downward) LW flux. The figures in the fifth row were obtained by subtracting the cloud-free LW heating rate obtained by running the radiation scheme without any clouds from the all-sky LW heating rate shown in the fourth row. The solid lines in each plot are (first row) a_c, (second row) a_s, (third row) a_r, and (fourth and fifth rows) a_c+a_s.

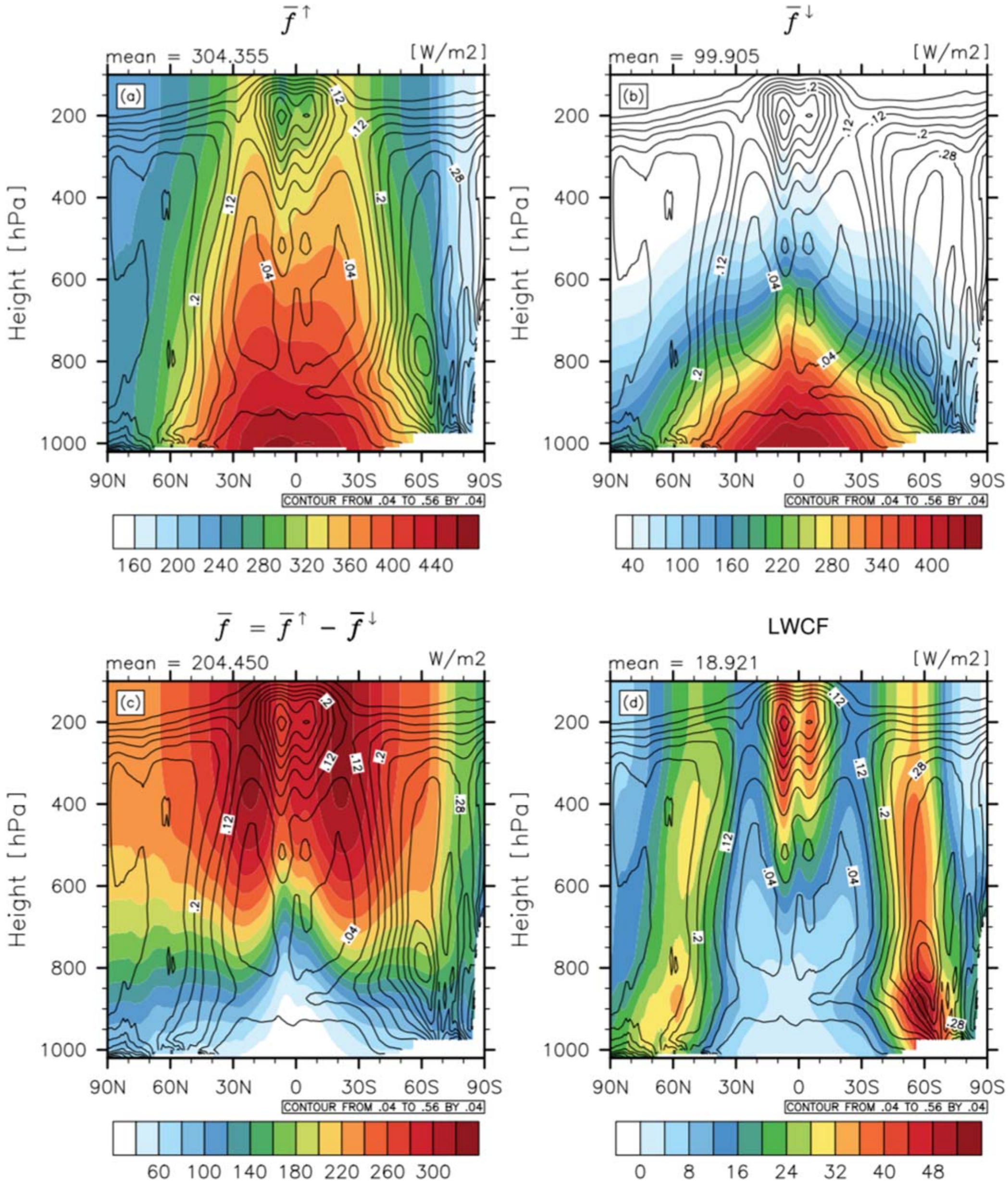

Figure 9. Annual zonal mean, grid mean (a) upward LW flux ($\bar{f}^{\uparrow}$), (b) downward LW flux ($\bar{f}^{\downarrow}$), (c) net upward LW flux ($\bar{f}=\bar{f}^{\uparrow}-\bar{f}^{\downarrow}$), and (d) LWCF. The solid line in each plot is a_c+a_s.

atmosphere below the clouds through abrupt enhancement of downward LW radiation across the cloud top (Figure 8n). This results in the destabilization of the atmospheric column in the subtropical and midlatitude lower tropospheres and, to a smaller degree, in the tropical upper troposphere (Figure 8o). Both upward and downward LW fluxes decrease with height, with maximum values in the tropical lower troposphere (Figures 9a and 9b), while the net upward LW flux increases with the height, with the maximum values at 25°N/S at the TOA. The LWCF at the TOA is maximal in the tropics and slightly smaller in the midlatitude storm track region. At the surface, however, the tropical LWCF is near zero and the maximum LWCF exists in midlatitude storm tracks.

4.2. Sensitivity Simulations

To evaluate the impacts of various simplifying assumptions for the vertical cloud overlap, which are frequently used in GCMs, a couple of sensitivity simulations were performed. First, the vertical stratus overlap was changed from the maximum-random overlap with an *e*-folding decorrelation length scale of stratus, $\Delta z_s=2$ km, to the maximum overlap ($\Delta z_s=\infty$) and random overlap ($\Delta z_s=0$). Similarly, the vertical cumulus overlap was changed from the maximum overlap to the maximum-random overlap with an *e*-folding decorrelation length scale of cumulus, $\Delta z_c=200$ m. Second, to mimic the treatment of clouds in the SAM0 radiation scheme, the radiation scheme was operated on a single cloud fraction $a=a_c+a_s$ and a single in-cloud condensate mass $\hat{q}_l=(a_c\hat{q}_{l,c}+a_s\hat{q}_{l,s})/(a_c+a_s)$ in each layer by assuming that the single cloud fraction a has the same maximum-random vertical overlap as stratus. Finally, to mimic the process-splitting treatment of convective and stratiform precipitations with IPA, as used in SAM0, two simulations were performed, namely, one by neglecting the heterogeneous accretion within cumulus and the other by neglecting the heterogeneous accretion within stratus. The precipitation resulting from the two simulations was added. Figure 10 shows the difference of the precipitation flux at the SFC and LWCF at the TOA between the sensitivity and control simulations. The zonal mean cross sections of corresponding precipitation and radiation fields are shown in Figures 11 and 12, respectively. One of the main goals of these sensitivity simulations is to examine whether any of the biases in the SAM0-simulated precipitation flux at the SFC and LWCF at the TOA (Figures 2d and 2h) are associated with various simplifying assumptions with respect to the vertical cloud overlap.

4.2.1. Maximum Versus Random Overlap

Compared with the control simulation, the maximum stratus overlap simulates a weaker LWCF at the TOA (Figure 10e), because the column-projected stratus coverage decreases from the control to the maximum stratus overlap. The random stratus overlap produces a similar pattern of ΔLWCF with an opposite sign (Figure 10f). The vertical cross section of ΔLWCF shows the strongest anomalies in the extratropical lower troposphere in which stratus is abundant (Figures 12c and 12f). Compared with the control simulation, the maximum stratus overlap increases the net upward LW flux at all heights and stabilizes the atmospheric column in the cloudy low troposphere and vice versa for random stratus overlap (Figures 12a, 12b, 12d, and 12e). Note the similarity between Figures 12e and 8o in the extratropical lower troposphere. Similar to the stratus, enhanced randomness of vertical cumulus overlap increases LWCF at all heights and destabilizes the lower troposphere (Figures10g, 12h, and 12i). Interestingly, the magnitude of the corresponding ΔLWCF is larger than that of stratus, although the cumulus fraction is much smaller than the stratus fraction. These anomalies of LWCF are consistent with our conceptual speculation that random cloud overlap increases the column-integrated cloud coverage and enhances the overall radiative impact of clouds.

In contrast to LWCF, the surface precipitation flux shows a somewhat unexpected response to the vertical stratus overlap. In the tropical deep convection region, the maximum stratus overlap simulates less surface precipitation flux than the random stratus overlap. Similar features, with an opposite sign, were observed for random stratus overlap. This contradicts our common speculation that the maximum stratus overlap simulates more precipitation flux than random stratus overlap due to stronger accretion within stratus and weaker evaporation of stratiform precipitation. To understand this unusual behavior, the anomalies of the total production rates of precipitation ($\Delta\bar{P}$) and the evaporation rate of precipitation ($\Delta\bar{E}_r$) were analyzed, as shown in Figure 11. Consistent with our common expectation, the maximum stratus overlap simulates stronger precipitation production than the control simulation in the midlatitude storm track region (Figure 11a). However, the maximum stratus overlap simulates more evaporation of precipitation, strong enough to compensate for the enhanced precipitation production in the tropical region (Figures 11b and 11c). Some a^M converted into a^C from control to maximum stratus overlap, which results in the increase of a_r^C and the associated grid mean evaporation rate of convective precipitation (not shown). This unexpected response of precipitation flux to the vertical stratus overlap is one of the unique aspects of dual cloud system: a single cloud system shows the opposite response to the vertical stratus overlap (not shown). In contrast to stratus, enhanced randomness of vertical cumulus overlap over the ocean produces less precipitation flux, which is mainly due to the increase of the evaporation rate of precipitation that is much larger than the increase of the precipitation production rate (Figures 10c and 11g–11i). Because our model does not parameterize accretion within cumulus, the enhanced randomness of cumulus overlap does not alter the accretion rate with cumulus but increases the production of mixed precipitation. If accretion within cumulus was included, the negative anomalies of the precipitation flux would have been further enhanced. The sign of surface precipitation flux anomalies over continents tends to be opposite of that over the ocean. Although the anomalies of the precipitation flux and LWCF have systematic geographical patterns, their overall magnitudes are quite small.

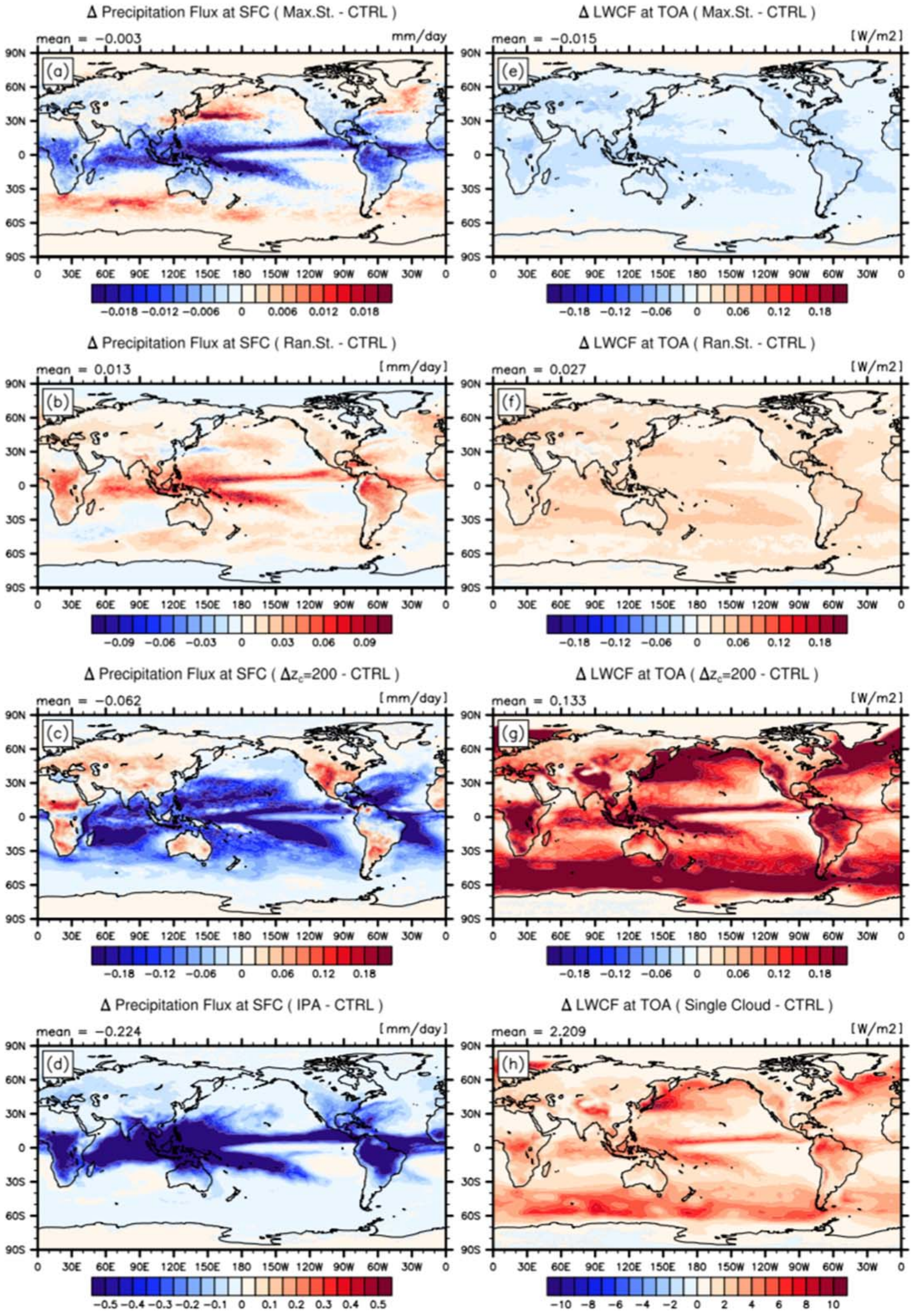

Figure 10. The difference maps of the (left) precipitation flux at the SFC and (right) LWCF at the TOA between the control simulation (CTRL: $\Delta z_s = 2,000$ (m) and $\Delta z_c = \infty$ with separate cumulus and stratus and the integrated treatment of convective and stratiform precipitation without IPA) and various sensitivity simulations for the (a, e) maximum stratus overlap ($\Delta z_s = \infty$), (b, f) random stratus overlap ($\Delta z_s = 0$), (c, g) maximum-random cumulus overlap ($\Delta z_c = 200$ (m)), (d) process-splitting sum with IPA, and (h) single-merged cloud.

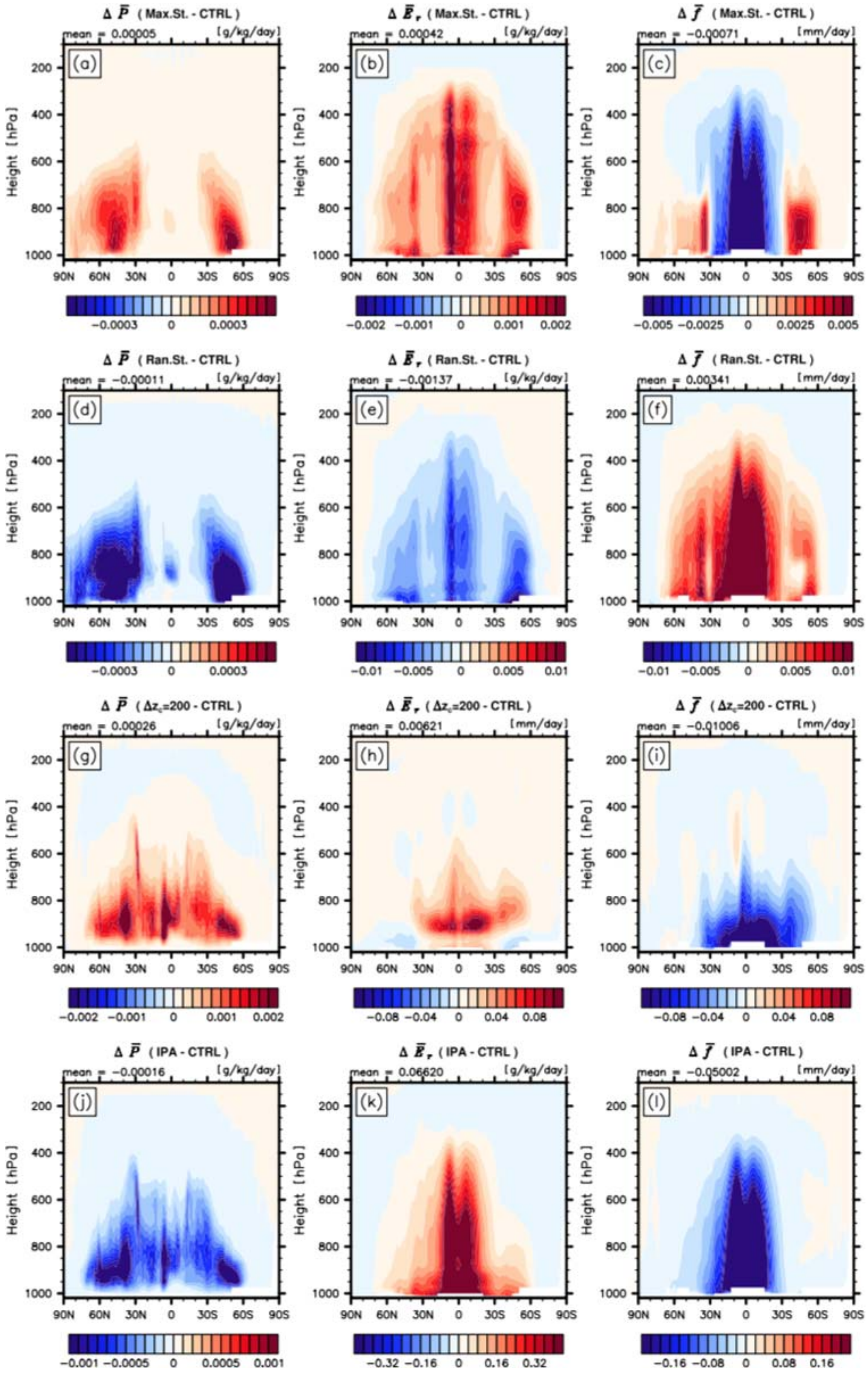

Figure 11. The difference of the (left) grid mean total production rate of precipitation ($\Delta\bar{P}$), (middle) grid mean evaporation rate of precipitation ($\Delta\bar{E}_r$), and (right) grid mean total precipitation flux ($\Delta\bar{f}$) between the control simulation and various sensitivity simulations for the (first row) maximum stratus overlap, (second row) random stratus overlap, (third row) maximum-random cumulus overlap ($\Delta z_c = 200\,(\mathrm{m})$), and (fourth row) process-splitting sum with IPA.

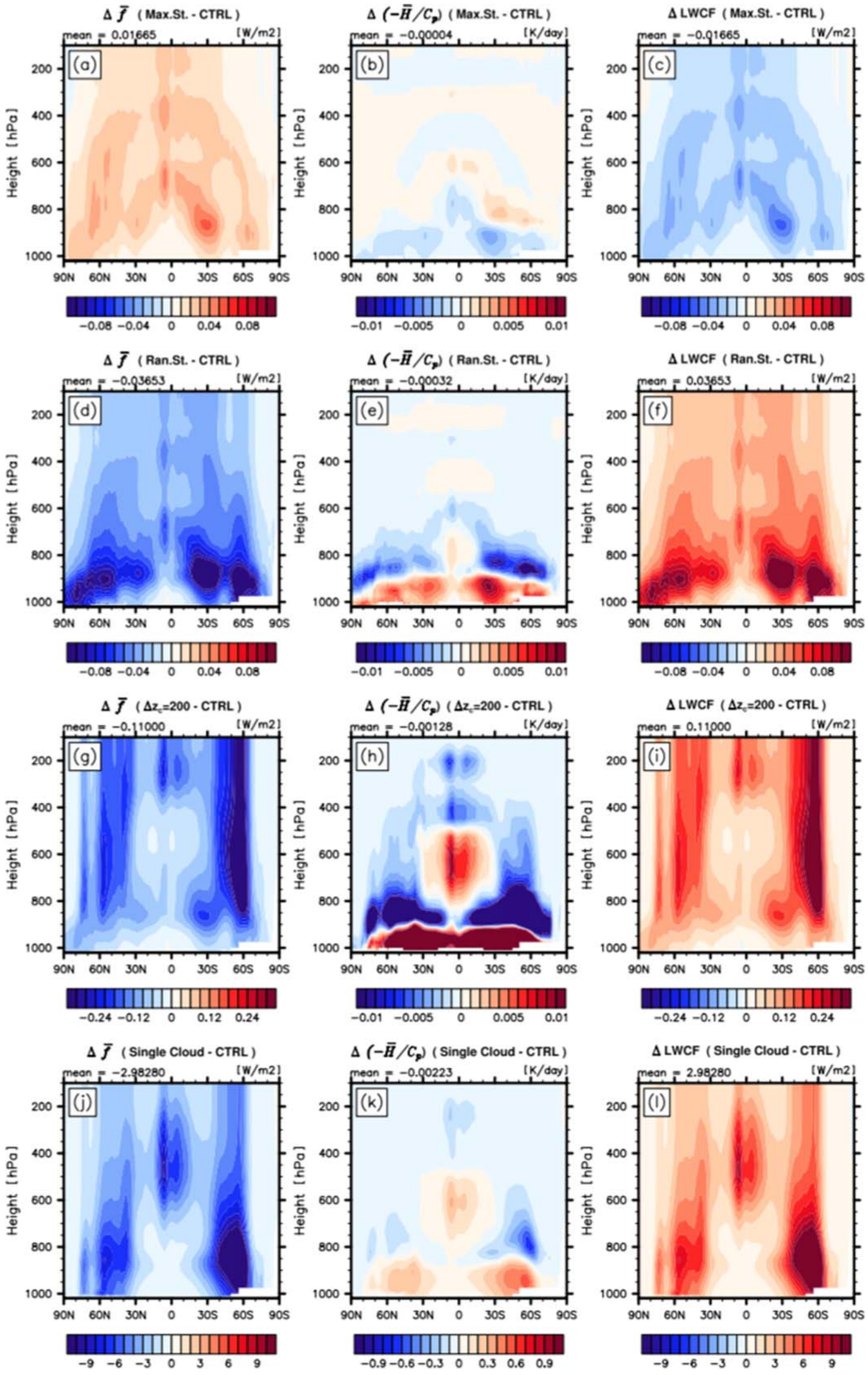

Figure 12. The difference of (left) net upward LW flux ($\Delta\bar{f}$), (middle) net LW heating rate ($\Delta(-\bar{H}/C_p)$), and (right) LWCF between the control simulation and various sensitivity simulations for the (first row) maximum stratus overlap, (second row) random stratus overlap, (third row) maximum-random cumulus overlap ($\Delta z_c = 200\,(\mathrm{m})$), and (fourth row) single-merged cloud.

4.2.2. Single Versus Dual Cloud Types

In many GCMs, multiple cloud types are combined into a single cloud and the radiation scheme is operating on the single cloud type. While this approach, to some degree, is inevitable because of several practical reasons (e.g., computational cost and the complexity of the default model structure), not much attention has been paid to potential biases associated with this simplified method. To explore this issue, a single cloud fraction $a = a_c + a_s$ and a single in-cloud condensate mass $\hat{q}_l = (a_c \hat{q}_{l,c} + a_s \hat{q}_{l,s})/(a_c + a_s)$ in each layer were defined by assuming that the single cloud fraction a follows the same maximum-random vertical overlap as a_s. In fact, this approximation is similar to that used in the SAM0 radiation scheme.

The simulation with a single-merged cloud that mimics the online radiation computation in SAM0 produces stronger LWCF at the TOA, particularly in the tropical deep convection and midlatitude storm track regions (Figure 10h). Compared with the control simulation, the net upward LW flux decreases and LWCF increases at all heights (Figures 12j and 12l) with the strongest anomalies in the southern hemispheric storm track region. The single cloud approximation is analogous to changing the vertical cumulus overlap from maximum to maximum-random, which results in the increase of the column-projected cloud coverage and associated LWCF. The pattern of the anomalous LW heating rate shown in Figure 12k is very similar to the cloud-induced LW heating rate in the control simulation (Figure 8o), indicating the destabilization of the extratropical low troposphere and tropical upper troposphere due to the single cloud approximation.

Although the cumulus fraction is much smaller than the stratus fraction, the magnitude of LWCF anomalies associated with the single cloud approximation is not negligible: the global mean LWCF anomaly is 2.2 (W m^{-2}), about 10% of the climatological LWCF, which is much larger than the anomalies associated with the maximum or random overlap of stratus and cumulus. Compared with the observation, SAM0 tends to simulate a stronger LWCF in the tropical deep convection and midlatitude storm track regions (Figure 2h). The comparison of Figure 2h with Figure 10h indicates that some of the positive biases in the SAM0-simulated LWCF are associated with the single cloud approximation of the radiation scheme.

4.2.3. Process-Splitting Treatment of Precipitations With IPA

To numerically stabilize the model with a long integration time step Δt, many GCMs use so-called process-splitting in which individual parameterization is applied to the updated state resulting from previous parameterization at each time step. In SAM0, the production and evaporation rates of convective precipitation are computed within the convection scheme, while those of stratiform precipitation are computed within the separate stratus microphysics scheme. When computing the production rate of precipitation, both schemes use an independent precipitation approximation (IPA), that is, the convection scheme neglects the precipitation production within stratus, the stratus microphysics scheme neglects the precipitation production within cumulus, and the evaporation is computed separately for each convective and stratiform precipitation. As a result, IPA does not generate mixed precipitation. Because of the practical difficulty in handling both convective and stratiform precipitation simultaneously within a single scheme, it is inevitable to use IPA in the process-splitting GCM; however, no studies have been performed to evaluate the validity of IPA. To check if IPA is an acceptable approach for the process-splitting GCM, two simulations were performed: one by tuning the precipitation production within stratus off to mimic the treatment of the precipitation process in the convection scheme; and the other by turning the precipitation production within cumulus off to mimic the treatment of the precipitation process in the stratus microphysics scheme. The precipitation from the two simulations was added and the resulting total precipitation fields were compared with those from the control simulation.

Overall, the process-splitting treatment of precipitation with IPA produces less surface precipitation flux than the control simulation, particularly in the tropical deep convection region (Figure 10d). Because heterogeneous accretion is neglected both in cumulus and stratus, the production rate of precipitation in the process-splitting simulation is weaker than that of the control simulation (Figure 11j). Interestingly, the evaporation rate of precipitation also increased (Figure 11k) because the separate sum of the evaporation rates of convective and stratiform precipitation is larger than the evaporation rate of the mixed evaporation. In the control simulation, the grid mean evaporation rate of mixed precipitation is computed as $\bar{E}_r^M = a_r^M \cdot k_e \cdot (1 - \hat{U}_r) \cdot \sqrt{\breve{f}^M}$, where $\hat{U}_r$ is the relative humidity in the clear portion and $\breve{f}^M$ is the precipitation flux within the mixed precipitation area (see Appendix D). During the process-splitting treatment, $\bar{E}_r^M$ is replaced by the sum of $\bar{E}_r^C$ and $\bar{E}_r^S$ with $\bar{E}_r^C = a_r^C \cdot k_e \cdot (1 - \hat{U}_r) \cdot \sqrt{\breve{f}^C}$ and $\bar{E}_r^S = a_r^S \cdot k_e \cdot (1 - \hat{U}_r) \cdot \sqrt{\breve{f}^S}$. In the case that $a_r^M = a_r^C = a_r^S$ and $\breve{f}^M = \breve{f}^C + \breve{f}^S$, it becomes $(\bar{E}_r^C + \bar{E}_r^S)/\bar{E}_r^M = \sqrt{3}$. Note that the pattern of Figure 11k is very similar to that of a_r^M (Figure 5i) and $\bar{f}^M$ (Figure 7c). The combined decrease of the production of precipitation and the increase of the evaporation of precipitation results in the decrease of precipitation flux from the control to the process-splitting simulation at all heights (Figure 11l). The comparison of Figure 10d with Figure 2d indicates that the process-splitting treatment of precipitation with IPA is not likely to be responsible for the biases in the SAM0-simulated precipitation rate at the SFC.

5. Summary and Conclusion

A heuristic parameterization was developed to handle the contrasting vertical overlap structures of cumulus and stratus in an integrated way. It is assumed that cumulus is maximum-randomly overlapped with adjacent cumulus with an *e*-folding decorrelation length scale Δz_c and stratus is maximum-randomly overlapped with adjacent stratus with an *e*-folding decorrelation length scale Δz_s. To handle the distinct radiative and cloud microphysical properties of cumulus and stratus with minimum computation cost, radiation and precipitation areas at each model interface were grouped into convective, stratiform, mixed, and clear-sky areas. The convective (stratiform, mixed) radiation area at the model interface is defined as the portion with a radiation flux that went through cumulus (stratus, both cumulus and stratus) or cumulus (stratus, both cumulus and stratus) and clear portions only. The remaining portion with a radiation flux that only passed through the clear sky is defined as clear radiation area. The four precipitation areas are defined in a similar way but with additional consideration of the evaporation of the precipitation within the clear sky. Any subarea variability of cloud and precipitation condensates within individual portions of cloud, radiation, and precipitation areas was neglected for simplicity.

The overlap parameterization was implemented into SAM0 in an offline mode. The global online SAM0 and offline control simulations were simultaneously run for 1 year in standalone mode and the simulation results were compared with the observation. To examine if any biases in the SAM0-simulated surface precipitation rate and LWCF at the TOA are associated with various simplifying assumptions with respect to the vertical cloud overlap, a couple of sensitivity simulations were performed with maximum and random stratus overlap instead of $\Delta z_s = 2,000\,(\mathrm{m})$, $\Delta z_c = 200\,(\mathrm{m})$ instead of $\Delta z_c = \infty$, radiation computation with a single-merged cloud instead of using separate cumulus and stratus, and process-splitting treatment of convective and stratiform precipitations with IPA.

The offline control simulation reasonably well reproduced the SAM0-simulated precipitation flux at the SFC and LWCF at the TOA. In the control simulation, a_c is one or two orders smaller than a_s, which is smaller than a_r. Similar to clouds, a^S is much larger than a^C, which is slightly smaller than a^M. In contrast to clouds, all precipitation and evaporation areas tend to decrease with the height. Because of the maximum cumulus overlap, convective precipitation above the cumulus base mainly falls into a_c^C, which is large in the tropical lower troposphere. On the other hand, a_s^S is large in the tropical upper troposphere and in the midlatitude storm track. The areas in which the mixed precipitation is initiated through heterogeneous accretion is much smaller than the areas where homogeneous accretion occurs ($a_s^C \ll a_c^C$, $a_c^S \ll a_s^S$). The clear-sky area without any clouds and precipitation is maximal in the midtroposphere at 25°N/S, where the Hadley circulation subsides, but it is minimal at 60°N/S near the surface, where midlatitude stork tracks exist. Although the cumulus fraction is much smaller than the stratus fraction, most of the precipitation in the tropical region is produced by cumulus, while the stratus contributes more in the midlatitude and tropical upper troposphere. The evaporation rate of precipitation is large in the tropical mid and lower troposphere, with a global mean evaporation rate of approximately one tenth of the global mean precipitation production rate. Most convective and mixed precipitation fluxes are concentrated in the tropical region, while a strong stratiform precipitation flux exists in midlatitude regions. The mixed precipitation flux is larger than the convective precipitation flux. The LWCF at the TOA is maximal in the tropics and midlatitude storm track regions; however, the LWCF at the SFC is near zero in the tropics. In contrast to the precipitation production, the global mean radiative heating by cumulus is much smaller than that of the stratus and clear sky. The net LW heating rate is strongly negative in the mid and lower troposphere, which is mainly due to the cooling by atmospheric water vapor. Because of radiative impacts, cloud condensates destabilize the atmosphere in the subtropical and midlatitude lower troposphere and, to a smaller degree, in the tropical upper troposphere.

Compared with the control simulation with $\Delta z_s = 2,000\ (\mathrm{m})$, the random stratus overlap with $\Delta z_s = 0$ simulates stronger LWCF because the column-projected stratus coverage increases from the control to the maximum stratus overlap. However, contradicting our common expectation, the precipitation flux also increases in response to less evaporation of precipitation, strong enough to compensate for the reduced precipitation production. It is likely that random stratus overlap decreases a_s^S but increases a_s^C, which results in the decrease of a_r^C and the associated evaporation of convective precipitation. This unexpected response of the precipitation flux to vertical stratus overlap is one of the unique aspects of a dual cloud system: a single cloud system shows the opposite response. Compared with the maximum cumulus overlap, the random cumulus overlap simulates stronger LWCF; however, in contrast to the stratus overlap, it simulates weaker precipitation flux, which is mainly due to enhanced evaporation. Compared with the control simulation with separate cumulus and stratus, the simulation with a single-merged cloud produces stronger LWCF at the TOA, particularly in the tropical deep convection and midlatitude storm track regions. Although the cumulus fraction of each layer is small, the magnitude of corresponding LWCF anomalies is large. It is likely that some positive biases of SAM0-simulated LWCF in the tropical deep convection and midlatitude storm track regions are associated with the single cloud approximation of the radiation scheme. Compared with the control simulation with mixed precipitation, the process-splitting treatment of convective and stratiform precipitation with IPA produces less precipitation flux at the SFC because the evaporation rate of precipitation increases due to the separate sum of evaporation rates of convective and stratiform precipitation and because the production rate of precipitation decreases due to the neglect of heterogeneous accretion.

For computational efficiency with physical rationality, the radiation and precipitation areas were grouped into four categories by assuming that there is no subarea variability within the individual area. However, previous studies noted the importance of subarea variability. By using more than four area categories, we can handle the subarea variability, in principle, which in fact becomes similar to the subcolumn approach. We can also take the nonlinear impact of subarea variability of in-cloud condensate within cumulus and stratus into account by computing the in-cloud radiative heating and in-cloud production rates of precipitation in a stochastic way. The successful application of the overlap parameterization depends on the GCM's ability to simulate the cloud fraction and in-cloud condensates of various cloud types in a realistic way. Park et al. (2017) showed that the addition of detrained cumulus to CAM5 substantially improved the simulations of low-level clouds and the associated short cloud radiative forcing. Continuous efforts are necessary to improve the simulations of cloud properties in GCMs. Finally, all dynamics and physics parameterization schemes (PBL, convection, cloud macrophysics, cloud microphysics, radiation, and aerosol wet deposition) should operate the identical cloud overlap structure, an issue the author is continuously working on.

Appendix A: Overlapping Areas Between Radiation (and Precipitation) and Cloud

In this section, a set of equations are provided for W_{tot}, i_{min}, i_{max}, and $W(i)$ for each four combinations of cumulus and stratus overlaps, which are used to compute the overlap area a_l^K in equation (4). The following combination and permutation operators are defined

$$ {}_{\alpha}C_{\beta} = \frac{\alpha!}{\beta!(\alpha-\beta)!}, \quad {}_{\alpha}P_{\beta} = \frac{\alpha!}{(\alpha-\beta)!}, \quad \alpha \geq \beta \geq 0, \tag{A1} $$

and

$$ n_c = N \cdot \min\left(a_c, a_{c\uparrow}\right), \tag{A2} $$

$$ n_s = N \cdot \min\left(a_s, a_{s\uparrow}\right), \tag{A3} $$

where $a_{c\uparrow}$ and $a_{s\uparrow}$ are stratus and cumulus fractions in the adjacent upper layers, respectively. equations (A2) and (A3) represent the conditions of maximum cumulus and maximum stratus overlap. The overlap area a_l^K consists of 12 components for $K = C, S, M, R$ and $l = c, s, r$. For the individual components, i_{min}, i_{max}, and $W(i)$ are computed by counting $Na_{l\uparrow}$ within Na^K and then computing the overlap area between $a_{l\uparrow}$ and a_l. The equation set derived in Appendix A is commonly used to compute both the downward radiation and precipitation given that a^K and $a_{l\uparrow}^K$ are separately obtained for each radiation and precipitation components, as will be discussed in Appendix B. In the case of upward radiation, the same equation set is used by replacing the upward arrow ↑ with the downward arrow ↓ that denotes the value in the adjacent lower layer.

A1. Maximum Cumulus and Maximum Stratus

In this case,

$$W_{tot}={}_{Na_c}C_{n_c}\cdot{}_{Na_{c\uparrow}}P_{n_c}\cdot{}_{Na_s}C_{n_s}\cdot{}_{Na_{s\uparrow}}P_{n_s}\cdot{}_{N-n_c-n_s}P_{N-n_c-n_s}. \tag{A4}$$

If $l=c$, the following is derived for $K=C,S,M,R$,

$$i_{\min}=\max\left[0,\ n_c-N(a_{c\uparrow}-a^K_{c\uparrow}),\ N(a^K+a_l-1)+\max(n_s-Na^K_{s\uparrow},0)\right], \tag{A5}$$

$$i_{\max}=\min\left[Na^K-\max(n_s-N(a_{s\uparrow}-a^K_{s\uparrow}),0),\ Na_l-\max(n_c-Na^K_{c\uparrow},0)\right], \tag{A6}$$

$$W(i)={}_{Na_c}C_{n_c}\cdot{}_{Na_s}C_{n_s}\cdot{}_{N(1-a_l)-n_s}P_{N(1-a_l)-n_s}\cdot w(i), \tag{A7}$$

$$\begin{aligned}w(i)=\sum_{j_s=j_{s,\min}}^{j_{s,\max}}\sum_{j_c=j_{c,\min}}^{j_{c,\max}}\Big[&{}_{n_c}C_{j_c}\cdot{}_{Na^K_{c\uparrow}}P_{j_c}\cdot{}_{N(a_{c\uparrow}-a^K_{c\uparrow})}P_{n_c-j_c}\cdot{}_{n_s}C_{j_s}\cdot{}_{Na^K_{s\uparrow}}P_{j_s}\cdot{}_{N(a_{s\uparrow}-a^K_{s\uparrow})}P_{n_s-j_s}\cdot{}_{Na_l-n_c}C_{i-j_c}\cdot{}_{Na^K-j_c-j_s}P_{i-j_c}\\&\cdot{}_{N(1-a^K)-(n_c-j_c)-(n_s-j_s)}P_{Na_l-n_c-i+j_c}\Big],\end{aligned} \tag{A8}$$

$$j_{c,\min}=\max\left[0,\ n_c-N(a_{c\uparrow}-a^K_{c\uparrow}),\ i+n_c-Na_l\right], \tag{A9}$$

$$j_{c,\max}=\min\left[n_c,\ Na^K_{c\uparrow},\ i\right], \tag{A10}$$

$$j_{s,\min}=\max\left[0,\ n_s-N(a_{s\uparrow}-a^K_{s\uparrow}),\ n_s-N(1-a^K-a_l)-i\right], \tag{A11}$$

$$j_{s,\max}=\min\left[n_s,\ Na^K_{s\uparrow},\ Na^K-i\right]. \tag{A12}$$

If $l=s$, the following can be derived

$$i_{\min}=\max\left[0,\ n_s-N(a_{s\uparrow}-a^K_{s\uparrow}),\ N(a^K+a_l-1)+\max(n_c-Na^K_{c\uparrow},0)\right], \tag{A13}$$

$$i_{\max}=\min\left[Na^K-\max(n_c-N(a_{c\uparrow}-a^K_{c\uparrow}),0),\ Na_l-\max(n_s-Na^K_{s\uparrow},0)\right], \tag{A14}$$

$$W(i)={}_{Na_c}C_{n_c}\cdot{}_{Na_s}C_{n_s}\cdot{}_{N(1-a_l)-n_c}P_{N(1-a_l)-n_c}\cdot w(i), \tag{A15}$$

$$\begin{aligned}w(i)=\sum_{j_s=j_{s,\min}}^{j_{s,\max}}\sum_{j_c=j_{c,\min}}^{j_{c,\max}}\Big[&{}_{n_c}C_{j_c}\cdot{}_{Na^K_{c\uparrow}}P_{j_c}\cdot{}_{N(a_{c\uparrow}-a^K_{c\uparrow})}P_{n_c-j_c}\cdot{}_{n_s}C_{j_s}\cdot{}_{Na^K_{s\uparrow}}P_{j_s}\cdot{}_{N(a_{s\uparrow}-a^K_{s\uparrow})}P_{n_s-j_s}\cdot\\&{}_{Na_l-n_s}C_{i-j_s}\cdot{}_{Na^K-j_c-j_s}P_{i-j_s}\cdot{}_{N(1-a^K)-(n_c-j_c)-(n_s-j_s)}P_{Na_l-n_s-i+j_s}\Big],\end{aligned} \tag{A16}$$

$$j_{c,\min}=\max\left[0,\ n_c-N(a_{c\uparrow}-a^K_{c\uparrow}),\ n_c-N(1-a^K-a_l)-i\right], \tag{A17}$$

$$j_{c,\max}=\min\left[n_c,\ Na^K_{c\uparrow},\ Na^K-i\right], \tag{A18}$$

$$j_{s,\min}=\max\left[0,\ n_s-N(a_{s\uparrow}-a^K_{s\uparrow}),\ i+n_s-Na_l\right], \tag{A19}$$

$$j_{s,\max}=\min\left[n_s,\ Na^K_{s\uparrow},\ i\right]. \tag{A20}$$

If $l=r$, the following can be derived

$$i_{\min}=\max\left[0,\ N(a^K+a_l-1)+\max(n_c-Na^K_{c\uparrow},0)+\max(n_s-Na^K_{s\uparrow},0)\right], \tag{A21}$$

$$i_{\max}=\min\left[Na_l,\ Na^K-\max(n_c-N(a_{c\uparrow}-a^K_{c\uparrow}),0)-\max(n_s-N(a_{s\uparrow}-a^K_{s\uparrow}),0)\right], \tag{A22}$$

$$W(i)={}_{Na_c}C_{n_c}\cdot{}_{Na_s}C_{n_s}\cdot{}_{Na_l}C_i\cdot{}_{N(1-a_l)-n_c-n_s}P_{N(1-a_l)-n_c-n_s}\cdot w(i), \tag{A23}$$

$$w(i)=\sum_{j_s=j_{s,\min}}^{j_{s,\max}}\sum_{j_c=j_{c,\min}}^{j_{c,\max}}\Big[\,{}_{n_c}C_{j_c}\cdot\ {}_{Na^K_{c\uparrow}}P_{j_c}\cdot\ {}_{N(a_{c\uparrow}-a^K_{c\uparrow})}P_{n_c-j_c}\cdot\ {}_{n_s}C_{j_s}\cdot\ {}_{Na^K_{s\uparrow}}P_{j_s}\cdot\ {}_{N(a_{s\uparrow}-a^K_{s\uparrow})}P_{n_s-j_s}$$
$$\cdot\ {}_{Na^K-j_c-j_s}P_i\cdot\ {}_{N(1-a^K)-(n_c-j_c)-(n_s-j_s)}P_{Na_l-i}\Big], \tag{A24}$$

$$j_{c,\min}=\max\left[0,\ n_c-N(a_{c\uparrow}-a^K_{c\uparrow}),\ N(a^K+a_l-1)+n_c+n_s-i-j_s\right], \tag{A25}$$

$$j_{c,\max}=\min\left[n_c,\ Na^K_{c\uparrow},\ Na^K-i-j_s\right], \tag{A26}$$

$$j_{s,\min}=\max\left[0,\ n_s-N(a_{s\uparrow}-a^K_{s\uparrow})\right], \tag{A27}$$

$$j_{s,\max}=\min\left[n_s,\ Na^K_{s\uparrow}\right]. \tag{A28}$$

A2. Maximum Cumulus and Random Stratus

In this case,

$$W_{tot}={}_{Na_c}C_{n_c}\cdot{}_{Na_{c\uparrow}}P_{n_c}\cdot{}_{N-n_c}P_{N-n_c}. \tag{A29}$$

If $l=c$, the following can be derived for $K=C, S, M, R$,

$$i_{\min}=\max\left[0,\ n_c-N(a_{c\uparrow}-a^K_{c\uparrow}),\ N(a^K+a_l-1)\right], \tag{A30}$$

$$i_{\max}=\min\left[Na^K,\ Na_l-\max\left(n_c-Na^K_{c\uparrow},0\right)\right], \tag{A31}$$

$$W(i)={}_{Na_c}C_{n_c}\cdot\ {}_{N(1-a_l)}P_{N(1-a_l)}\cdot\ w(i), \tag{A32}$$

$$w(i)=\sum_{j_c=j_{c,\min}}^{j_{c,\max}}\Big[\,{}_{n_c}C_{j_c}\cdot\ {}_{Na^K_{c\uparrow}}P_{j_c}\cdot\ {}_{N(a_{c\uparrow}-a^K_{c\uparrow})}P_{n_c-j_c}\cdot\ {}_{Na_l-n_c}C_{i-j_c}\cdot\ {}_{Na^K-j_c}P_{i-j_c}\cdot\ {}_{N(1-a^K)-n_c+j_c}P_{Na_l-n_c-i+j_c}\Big], \tag{A33}$$

$$j_{c,\min}=\max\left[0,\ n_c-N(a_{c\uparrow}-a^K_{c\uparrow}),\ i+n_c-Na_l\right], \tag{A34}$$

$$j_{c,\max}=\min\left[n_c,\ Na^K_{c\uparrow},\ i\right]. \tag{A35}$$

If $l=s, r$, the following can be derived

$$i_{\min}=\max\left[0,\ N(a^K+a_l-1)+\max\left(n_c-Na^K_{c\uparrow},0\right)\right], \tag{A36}$$

$$i_{\max}=\min\left[Na_l,\ Na^K-\max\left(n_c-N(a_{c\uparrow}-a^K_{c\uparrow}),0\right)\right], \tag{A37}$$

$$W(i)={}_{Na_l}C_i\cdot\ {}_{Na_c}C_{n_c}\cdot\ {}_{N(1-a_l)-n_c}P_{N(1-a_l)-n_c}\cdot\ w(i), \tag{A38}$$

$$w(i)=\sum_{j_c=j_{c,\min}}^{j_{c,\max}}\Big[\,{}_{n_c}C_{j_c}\cdot\ {}_{Na^K_{c\uparrow}}P_{j_c}\cdot\ {}_{N(a_{c\uparrow}-a^K_{c\uparrow})}P_{n_c-j_c}\cdot\ {}_{Na^K-j_c}P_i\cdot\ {}_{N(1-a^K)-n_c+j_c}P_{Na_l-i}\Big], \tag{A39}$$

$$j_{c,\min}=\max\left[0,\ n_c-N(a_{c\uparrow}-a^K_{c\uparrow}),\ N(a^K+a_l-1)+n_c-i\right], \tag{A40}$$

$$j_{c,\max}=\min\left[n_c,\ Na^K_{c\uparrow},\ Na^K-i\right]. \tag{A41}$$

A3. Random Cumulus and Maximum Stratus

In this case,

$$W_{tot}={}_{Na_s}C_{n_s}\cdot{}_{Na_{s\uparrow}}P_{n_s}\cdot{}_{N-n_s}P_{N-n_s}. \tag{A42}$$

If $l=s$, the following can be derived for $K=C, S, M, R$,

$$i_{\min}=\max\left[0,\ n_s-N(a_{s\uparrow}-a^K_{s\uparrow}),\ N(a^K+a_l-1)\right], \tag{A43}$$

$$i_{\max}=\min\left[Na^K,\ Na_l-\max\left(n_s-Na^K_{s\uparrow},0\right)\right], \tag{A44}$$

$$W(i) = {}_{Na_s}C_{n_s} \cdot {}_{N(1-a_l)}P_{N(1-a_l)} \cdot w(i), \tag{A45}$$

$$w(i) = \sum_{j_s=j_{s,\min}}^{j_{s,\max}} \left[{}_{n_s}C_{j_s} \cdot {}_{Na^K_{s\uparrow}}P_{j_s} \cdot {}_{N(a_{s\uparrow}-a^K_{s\uparrow})}P_{n_s-j_s} \cdot {}_{Na_l-n_s}C_{i-j_s} \cdot {}_{Na^K-j_s}P_{i-j_s} \cdot {}_{N(1-a^K)-n_s+j_s}P_{Na_l-n_s-i+j_s} \right], \tag{A46}$$

$$j_{s,\min} = \max\left[0,\ n_s - N(a_{s\uparrow}-a^K_{s\uparrow}),\ i+n_s-Na_l\right], \tag{A47}$$

$$j_{s,\max} = \min\left[n_s,\ Na^K_{s\uparrow},\ i\right]. \tag{A48}$$

If $l=c, r$, the following can be derived

$$i_{\min} = \max\left[0,\ N(a^K+a_l-1) + \max\left(n_s - Na^K_{s\uparrow}, 0\right)\right], \tag{A49}$$

$$i_{\max} = \min\left[Na_l,\ Na^K - \max\left(n_s - N(a_{s\uparrow}-a^K_{s\uparrow}), 0\right)\right], \tag{A50}$$

$$W(i) = {}_{Na_l}C_i \cdot {}_{Na_s}C_{n_s} \cdot {}_{N(1-a_l)-n_s}P_{N(1-a_l)-n_s} \cdot w(i), \tag{A51}$$

$$w(i) = \sum_{j_s=j_{s,\min}}^{j_{s,\max}} \left[{}_{n_s}C_{j_s} \cdot {}_{Na^K_{s\uparrow}}P_{j_s} \cdot {}_{N(a_{s\uparrow}-a^K_{s\uparrow})}P_{n_s-j_s} \cdot {}_{Na^K-j_s}P_i \cdot {}_{N(1-a^K)-n_s+j_s}P_{Na_l-i} \right], \tag{A52}$$

$$j_{s,\min} = \max\left[0,\ n_s - N(a_{s\uparrow}-a^K_{s\uparrow}),\ N(a^K+a_l-1)+n_s-i\right], \tag{A53}$$

$$j_{s,\max} = \min\left[n_s,\ Na^K_{s\uparrow},\ Na^K-i\right]. \tag{A54}$$

A4. Random Cumulus and Random Stratus

In this case,

$$W_{tot} = {}_NP_N. \tag{A55}$$

For each $l=c, s, r$, the following can be derived for $K=C, S, M, R$,

$$i_{\min} = \max\left[0,\ N(a^K+a_l-1)\right], \tag{A56}$$

$$i_{\max} = \min\left[Na_l,\ Na^K\right], \tag{A57}$$

$$W(i) = {}_{Na_l}C_i \cdot {}_{N(1-a_l)}P_{N(1-a_l)} \cdot {}_{Na^K}P_i \cdot {}_{N(1-a^K)}P_{Na_l-i}. \tag{A58}$$

Appendix B: Computation of Radiation Areas and Radiation Fluxes

To finish the computation of a^K_l in Appendix A, we need to compute $a^K_{c\uparrow}$ ($a^K_{s\uparrow}$), the overlap area between cumulus (stratus) in the adjacent upper layer and the radiation area at the top interface of the current layer. In the case of radiation, assuming that clear sky ($l = r$) has a LW absorptivity smaller than 1, the following can be computed:

$$\begin{aligned} a^C_{c\uparrow} &= a^{C\uparrow}_{c\uparrow} + a^{R\uparrow}_{c\uparrow}, \\ a^S_{c\uparrow} &= 0, \\ a^M_{c\uparrow} &= a^{S\uparrow}_{c\uparrow} + a^{M\uparrow}_{c\uparrow}, \\ a^R_{c\uparrow} &= 0, \end{aligned} \tag{B1}$$

where the upper arrow ↑ denotes the values in the adjacent upper layer or upper interface (see Figure 1). Because the computation is sequentially performed from the top layer to the bottom layer for downward radiation (and vice versa for upward radiation), $a^{K\uparrow}_{l\uparrow}$ is already known for all combinations of $K=C, S, M, R$ and $l=c, r, s$. In a similar way, $a^K_{s\uparrow}$ can be computed as follows:

$$\begin{aligned}
a_{s\uparrow}^{C} &= 0,\\
a_{s\uparrow}^{S} &= a_{s\uparrow}^{S\uparrow} + a_{s\uparrow}^{R\uparrow},\\
a_{s\uparrow}^{M} &= a_{s\uparrow}^{C\uparrow} + a_{s\uparrow}^{M\uparrow},\\
a_{s\uparrow}^{R} &= 0,
\end{aligned} \tag{B2}$$

Based on this, the computation of a_l^K was completed for all 12 combinations of $K=C, S, M, R$ and $l=c, r, s$ in each layer for radiation. The next step is to compute the radiation areas at the base interface $a^{K\downarrow}$, where the downward arrow denotes the base interface of the individual grid layer (Figure 1). By assuming that clear sky ($l=r$) has a LW absorptivity smaller than 1, $a^{K\downarrow}$ can be computed as follows:

$$\begin{aligned}
a^{C\downarrow} &= a_c^C + a_r^C + a_c^R,\\
a^{S\downarrow} &= a_s^S + a_r^S + a_s^R,\\
a^{M\downarrow} &= a_c^M + a_s^M + a_r^M + a_s^C + a_c^S,\\
a^{R\downarrow} &= a_r^R.
\end{aligned} \tag{B3}$$

The final step is to compute the grid mean production rates of radiation $\bar{H}_l$ and the grid mean radiation flux at the base interface $\bar{f}^{K\downarrow}$. The grid mean production rates of radiation from cumulus ($\bar{H}_c$), stratus ($\bar{H}_s$), and clear sky ($\bar{H}_r$) are

$$\begin{aligned}
\bar{H}_c &= a_c^C \hat{H}_c^C + a_c^S \hat{H}_c^S + a_c^M \hat{H}_c^M + a_c^R \hat{H}_c^R,\\
\bar{H}_s &= a_s^C \hat{H}_s^C + a_s^S \hat{H}_s^S + a_s^M \hat{H}_s^M + a_s^R \hat{H}_s^R,\\
\bar{H}_r &= a_r^C \hat{H}_r^C + a_r^S \hat{H}_r^S + a_r^M \hat{H}_r^M + a_r^R \hat{H}_r^R,
\end{aligned} \tag{B4}$$

where $\hat{H}_l^K$ is the in-cloud production rate of radiation when the radiation flux in the Kth radiation area falls into the lth cloud at the layer midpoint. Appendix D provides an explanation on how to compute $\hat{H}_l^K$. The grid mean radiation fluxes at the base interface for convective ($\bar{f}^{C\downarrow}$), stratiform ($\bar{f}^{S\downarrow}$), mixed ($\bar{f}^{M\downarrow}$), and clear-sky ($\bar{f}^{R\downarrow}$) radiation components are

$$\begin{aligned}
\bar{f}^{C\downarrow} &= \bar{f}^{C} - a_s^C \breve{f}^{C} + a_c^R \breve{f}^{R} + (a_c^C \hat{H}_c^C + a_c^R \hat{H}_c^R + a_r^C \hat{H}_r^C)\cdot(\Delta p/g),\\
\bar{f}^{S\downarrow} &= \bar{f}^{S} - a_c^S \breve{f}^{S} + a_s^R \breve{f}^{R} + (a_s^S \hat{H}_s^S + a_s^R \hat{H}_s^R + a_r^S \hat{H}_r^S)\cdot(\Delta p/g),\\
\bar{f}^{M\downarrow} &= \bar{f}^{M} + a_s^C \breve{f}^{C} + a_c^S \breve{f}^{S} + (a_s^C \hat{H}_s^C + a_c^S \hat{H}_c^S + a_c^M \hat{H}_c^M + a_s^M \hat{H}_s^M + a_r^M \hat{H}_r^M)\cdot(\Delta p/g),\\
\bar{f}^{R\downarrow} &= \bar{f}^{R} - a_c^R \breve{f}^{R} - a_s^R \breve{f}^{R} + (a_r^R \hat{H}_r^R)\cdot(\Delta p/g),
\end{aligned} \tag{B5}$$

where Δp is the pressure thickness of the grid layer, $\bar{f}^K$ is the grid mean radiation flux at the top interface, and $\breve{f}^K = \bar{f}^K / a^K$ is the radiation flux at the top interface within an individual radiation area. The same equation set is used to compute upwelling radiation by switching the downward arrow ↓ that denotes the values in the adjacent lower interface to the upward arrow ↑ that denotes the values in the adjacent upper interface.

Appendix C: Computation of Precipitation Areas and Precipitation Fluxes

The precipitation can be treated in a similar way as radiation. However, the following two situations need to be carefully handled: (1) no additional precipitation is generated when convective (stratiform) precipitation falls into stratus (cumulus) and (2) convective or stratiform precipitation falling into the clear portion completely evaporates. In the case of radiation, the convective radiation flux passing down stratus is always identified as mixed radiation at the base interface because stratus has a positive LW emissivity. In the case of precipitation, however, convective precipitation flux passing down stratus will be identified as convective precipitation at the base interface if additional precipitation is not generated within the stratus. In addition, radiation flux passing through the clear sky is not depleted; however, precipitation flux falling into the clear portion can completely evaporate. By taking these facts into account, $a_{c\uparrow}^{K}$ for the precipitation with cumulus can be computed as follows:

$$\begin{aligned}
a_{c\uparrow}^{C} &= a_{c\uparrow}^{C\uparrow} + a_{c\uparrow}^{R\uparrow} \cdot \epsilon_{c\uparrow},\\
a_{c\uparrow}^{S} &= a_{c\uparrow}^{S\uparrow} \cdot (1-\gamma_{c\uparrow}^{S\uparrow}) \cdot (1-\epsilon_{c\uparrow}),\\
a_{c\uparrow}^{M} &= a_{c\uparrow}^{M\uparrow} + a_{c\uparrow}^{S\uparrow} \cdot [1-(1-\gamma_{c\uparrow}^{S\uparrow}) \cdot (1-\epsilon_{c\uparrow})],\\
a_{c\uparrow}^{R} &= a_{c\uparrow}^{R\uparrow} \cdot (1-\epsilon_{c\uparrow}),
\end{aligned} \tag{C1}$$

where $\epsilon_{c\uparrow}=1$ (0) if cumulus in the adjacent upper layer does (not) generate convective precipitation by autoconversion and $\gamma_{c\uparrow}^{S\uparrow}=1$ (0) if stratiform precipitation falling into cumulus in the adjacent upper layer does (not) generate mixed precipitation by accretion. Similarly, the equations for the precipitation with stratus are

$$\begin{aligned}
a_{s\uparrow}^{C} &= a_{s\uparrow}^{C\uparrow} \cdot (1-\gamma_{s\uparrow}^{C\uparrow}) \cdot (1-\epsilon_{s\uparrow}),\\
a_{s\uparrow}^{S} &= a_{s\uparrow}^{S\uparrow} + a_{s\uparrow}^{R\uparrow} \cdot \epsilon_{s\uparrow},\\
a_{s\uparrow}^{M} &= a_{s\uparrow}^{M\uparrow} + a_{s\uparrow}^{C\uparrow} [1-(1-\gamma_{s\uparrow}^{C\uparrow}) \cdot (1-\epsilon_{s\uparrow})],\\
a_{s\uparrow}^{R} &= a_{s\uparrow}^{R\uparrow} \cdot (1-\epsilon_{s\uparrow}),
\end{aligned} \tag{C2}$$

where $\epsilon_{s\uparrow}=1$ (0) if stratus in the adjacent upper layer does (not) generate stratiform precipitation by autoconversion and $\gamma_{s\uparrow}^{C\uparrow}=1$ (0) if convective precipitation falling into stratus in the adjacent upper layer does (not) generate mixed precipitation by accretion.

Based on this, the computation of a_{l}^{K} for precipitation was completed. Subsequently, the precipitation areas at the base interface $a^{K\downarrow}$ can be computed as follows:

$$\begin{aligned}
a^{C\downarrow} &= a_{c}^{C} + a_{s}^{C} \cdot (1-\gamma_{s}^{C}) \cdot (1-\epsilon_{s}) + a_{r}^{C} \cdot (1-\delta^{C}) + a_{c}^{R} \cdot \epsilon_{c},\\
a^{S\downarrow} &= a_{s}^{S} + a_{c}^{S} \cdot (1-\gamma_{c}^{S}) \cdot (1-\epsilon_{c}) + a_{r}^{S} \cdot (1-\delta^{S}) + a_{s}^{R} \cdot \epsilon_{s},\\
a^{M\downarrow} &= a_{c}^{M} + a_{s}^{M} + a_{r}^{M} \cdot (1-\delta^{M}) + a_{s}^{C} \cdot [1-(1-\gamma_{s}^{C}) \cdot (1-\epsilon_{s})] + a_{c}^{S} \cdot [1-(1-\gamma_{c}^{S}) \cdot (1-\epsilon_{c})],\\
a^{R\downarrow} &= a_{r}^{R} + a_{r}^{C} \cdot \delta^{C} + a_{r}^{S} \cdot \delta^{S} + a_{r}^{M} \cdot \delta^{M} + a_{c}^{R} \cdot (1-\epsilon_{c}) + a_{s}^{R} \cdot (1-\epsilon_{s}),
\end{aligned} \tag{C3}$$

where $\epsilon_{l}=1$ (0) if new precipitation is (not) generated by autoconverion with cloud a_{l}, $\gamma_{l}^{K}=1$ (0) if mixed precipitation is (not) generated by heterogeneous accretion, and $\delta^{K}=1$ (0) if the precipitation flux at the top interface $\breve{f}^{K}$ (not) completely evaporates in the clear sky. As an example, if convective precipitation falling into stratus does not generate mixed precipitation by heterogeneous accretion, $\gamma_{s}^{C}=0$. Similarly, if stratiform precipitation falling into cumulus does not generate mixed precipitation by heterogeneous accretion, $\gamma_{c}^{S}=0$. If $\epsilon_{l}=1$, $\gamma_{l}^{K}=1$ and $\delta^{K}=0$, equation (C3) becomes identical to equation (B3).

The grid mean production rates of precipitation from cumulus ($\bar{P}_{c}$) and stratus ($\bar{P}_{s}$) and the grid mean evaporation rate of precipitation in the clear sky ($\bar{E}_{r}$) are

$$\begin{aligned}
\bar{P}_{c} &= a_{c}^{C}\hat{P}_{c}^{C} + a_{c}^{S}\hat{P}_{c}^{S} + a_{c}^{M}\hat{P}_{c}^{M} + a_{c}^{R}\hat{P}_{c}^{R},\\
\bar{P}_{s} &= a_{s}^{C}\hat{P}_{s}^{C} + a_{s}^{S}\hat{P}_{s}^{S} + a_{s}^{M}\hat{P}_{s}^{M} + a_{s}^{R}\hat{P}_{s}^{R},\\
\bar{E}_{r} &= a_{r}^{C}\hat{E}_{r}^{C} + a_{r}^{S}\hat{E}_{r}^{S} + a_{r}^{M}\hat{E}_{r}^{M} + a_{r}^{R}\hat{E}_{r}^{R},
\end{aligned} \tag{C4}$$

where $\hat{P}_{l}^{K}$ is the in-cloud production rate of precipitation when $\breve{f}^{K}$ falls into a_{l} and $\hat{E}_{r}^{K}$ is the evaporation rate of precipitation within the clear portion when $\breve{f}^{K}$ falls into a_{r}. Appendix D provides an explanation on how to compute $\hat{P}_{l}^{K}$ and $\hat{E}_{r}^{K}$. The grid mean precipitation fluxes at the base interface for convective ($\bar{f}^{C\downarrow}$), stratiform ($\bar{f}^{S\downarrow}$), mixed ($\bar{f}^{M\downarrow}$), and clear-sky ($\bar{f}^{R\downarrow}$) precipitation components are

$$
\begin{aligned}
&\bar{f}^{C\downarrow}=\bar{f}^{C}-a_s^C\breve{f}^{C}\cdot[1-(1-\gamma_s^C)\cdot(1-\epsilon_s)]+(a_c^C\hat{P}_c^C+a_c^R\hat{P}_c^R-a_r^C\hat{E}_r^C)\cdot(\Delta p/g),\\
&\bar{f}^{S\downarrow}=\bar{f}^{S}-a_c^S\breve{f}^{S}\cdot[1-(1-\gamma_c^S)\cdot(1-\epsilon_c)]+(a_s^S\hat{P}_s^S+a_s^R\hat{P}_s^R-a_r^S\hat{E}_r^S)\cdot(\Delta p/g),\\
&\bar{f}^{M\downarrow}=\bar{f}^{M}+a_s^C\breve{f}^{C}\cdot[1-(1-\gamma_s^C)\cdot(1-\epsilon_s)]+a_c^S\breve{f}^{S}\cdot[1-(1-\gamma_c^S)\cdot(1-\epsilon_c)]\\
&+(a_s^C\hat{P}_s^C+a_c^S\hat{P}_c^S+a_c^M\hat{P}_c^M+a_s^M\hat{P}_s^M-a_r^M\hat{E}_r^M)\cdot(\Delta p/g),\\
&\bar{f}^{R\downarrow}=\bar{f}^{R}-(a_r^R\hat{E}_r^R)\cdot(\Delta p/g)=0.
\end{aligned}
\tag{C5}
$$

Appendix D: Radiation Production Rate and the Production and Evaporation Rates of Precipitation

For simplicity, it was assumed that only liquid condensate exists within cumulus and stratus. The absorption coefficient of the individual cloud $\hat{k}_{abs,l}$ for $l=c,s,r$ is $\hat{k}_{abs,l}=\sum_i q(i)\cdot k_{abs}(i)$, where $q(i)$ is the specific mass and $k_{abs}(i)$ is the absorption cross section of the individual component i that consists of cloud condensate, water vapor, dry air, and other trace gases. The emissivity and absorptivity of the cloud component l is $1-\exp(-\hat{k}_{abs,l}\cdot\Delta p/g)$. The in-cloud net production rate of LW radiation $\hat{H}_l^K$ in $(\mathrm{J\,s^{-1}\,kg^{-1}})$ when the radiation flux $\breve{f}^{K}$ falls into the cloud is

$$
\hat{H}_l^K=(\sigma T^4-\breve{f}^{K})\cdot[1-\exp(-\hat{k}_{abs,l}\cdot\Delta p/g)]\cdot\left(\frac{g}{\Delta p}\right),
\tag{D1}
$$

where $\sigma=5.67\times10^{-8}\,(\mathrm{W\,m^{-2}\,K^{-4}})$ is the Stefan-Boltzmann constant and T is the temperature that is assumed to be horizontally uniform within the grid layer. For simplicity, the absorption cross sections of dry air and other trace gases were neglected. The absorption cross section of in-cloud condensate and water vapor are set to 150 and $0.16\,(\mathrm{m^2\,kg^{-1}})$, respectively, so that $\hat{k}_{abs,c}=150\cdot\hat{q}_{l,c}+0.16\cdot\bar{q}_v$ and $\hat{k}_{abs,s}=150\cdot\hat{q}_{l,s}+0.16\cdot\bar{q}_v$, where $\hat{q}_{l,c}$ and $\hat{q}_{l,s}$ are the in-cloud liquid water contents (LWC) of cumulus and stratus, respectively, and $\bar{q}_v$ is the grid mean water vapor that is assumed to be horizontally uniform within the grid layer. The radiative heating rate in $(\mathrm{K\,s^{-1}})$ is $\hat{Q}_l^K=-\hat{H}_l^K/C_p$, where $C_p=1,004\,(\mathrm{J\,kg^{-1}\,K^{-1}})$ is the specific heat of the atmosphere at constant pressure.

Following the treatment in the SAM0 stratus microphysics scheme, precipitation within stratus can be generated by either autoconversion or accretion processes. The in-stratus production rate of precipitation in $(\mathrm{kg\,kg^{-1}\,s^{-1}})$ is computed as

$$
\hat{P}_s^K=7.3\times10^{20}\cdot\hat{q}_{l,s}^{0.68}\cdot r_e^{5.37}\cdot\rho_a^{-1.79}+71.9\cdot\left(\hat{q}_{l,s}\cdot\frac{\breve{f}^{K}}{V_t\cdot\rho_a}\right)^{1.15},
\tag{D2}
$$

where $r_e=15.1\times10^{-6}\,(\mathrm{m})$ is the effective radius of the cloud liquid droplet, $V_t=8$ and $2\,(\mathrm{m\,s^{-1}})$ are the terminal fall velocities of convective and stratiform precipitation droplets, respectively, $\hat{q}_{l,s}$ is the in-stratus LWC, and ρ_a is the air density. The first and second terms on the RHS denote autoconversion and accretion processes, respectively.

Following the treatment in UNICON, precipitation within cumulus can be generated by an autoconversion process only. The in-cumulus production rate of precipitation in $(\mathrm{kg\,kg^{-1}\,s^{-1}})$ is computed as

$$
\hat{P}_c^K=-\hat{w}\cdot c_{at}\cdot\max[\left(1-\frac{\hat{q}_{l,crit}}{\hat{q}_{l,c}}\right),0]\cdot\hat{q}_{l,c},
\tag{D3}
$$

where c_{at} is an autoconversion efficiency that is set to 4×10^{-3} and $2\times10^{-3}\,(\mathrm{m^{-1}})$ over the ocean and land, respectively, $\hat{w}$ is the vertical velocity of convective updraft plume, g is the gravitational acceleration, $\hat{q}_{l,c}$ is the in-cumulus LWC, and $\hat{q}_{l,crit}=0.6\,(\mathrm{g\,kg^{-1}})$ is the maximum in-cumulus condensate that cumulus can hold prior to the precipitation production. An upper bound is imposed on $\hat{P}_s^K$ and $\hat{P}_c^K$ such that equations (D2) and (D3) do not precipitate more than the available cloud condensate mass.

Following the treatment in SAM0, the evaporation rate of precipitation within the clear portion in $(\mathrm{kg\,kg^{-1}}$ $\mathrm{s^{-1}})$ is computed as

$$\hat{E}_r^K = k_e \cdot (1 - \hat{U}_r) \cdot \sqrt{\breve{f}^K}, \tag{D4}$$

where $k_e = 3 \times 10^{-5}$ and 2×10^{-6} $(\mathrm{m(kg\,s)}^{-0.5})$ are the evaporation efficiencies of convective and stratiform precipitation, respectively, and $\hat{U}_r$ is the relative humidity of the clear portion. An upper bound is imposed on $\hat{E}_r^K$ such that equation (D4) does not evaporate more than the available precipitation flux. The terminal velocity and evaporation efficiency of the mixed precipitation are computed by the precipitation flux weighting averages of those of convective and stratiform precipitation.

Acknowledgments

This work was supported by Creative-Pioneering Researchers Program of the Seoul National University (SNU; grant 3345-20170017). The author expresses his thanks to Siyun Kim for her help in preparing the plots. The data used in this paper are available at http://nmlab.snu.ac.kr/datapublic/james2017b/.

References

Barker, H., Stephens, G. L., Partain, P. T., Bergman, J. W., Bonnel, B., Campana, K., . . . Yang, F. (2003). Assessing 1D atmospheric solar radiative transfer models: Interpretation and handling of unresolved clouds. *Journal of Climate*, *16*(16), 2676–2699.

Barker, H. W. (2008a). Overlap of fractional cloud for radiation calculations in gcms: A global analysis using cloudsat and calipso data. *Journal of Geophysical Research*, *113*, D00A01. https://doi.org/10.1029/2007JD009677

Barker, H. W. (2008b). Representing cloud overlap with an effective decorrelation length: An assessment using cloudsat and calipso data. *Journal of Geophysical Research*, *113*, D24205. https://doi.org/10.1029/2008JD010391

Barker, H. W., Stephens, G. L., & Fu, Q. (1999). The sensitivity of domain-averaged solar fluxes to assumptions about cloud geometry. *Quarterly Journal of the Royal Meteorological Society*, *125*(558), 2127–2152.

Bretherton, C. S., & Park, S. (2009). A new moist turbulence parameterization in the community atmosphere model. *Journal of Climate*, *22*(12), 3422–3448.

Brooks, M. E., Hogan, R. J., & Illingworth, A. J. (2005). Parameterizing the difference in cloud fraction defined by area and by volume as observed with radar and lidar. *Journal of the Atmospheric Sciences*, *62*(7), 2248–2260.

Collins, W. D. (2001). Parameterization of generalized cloud overlap for radiative calculations in General Circulation Models. *Journal of the Atmospheric Sciences*, *58*(21), 3224–3242.

Corbetta, G., Orlandi, E., Heus, T., Neggers, R., & Crewell, S. (2015). Overlap statistics of shallow boundary layer clouds: Comparing ground-based observations with large-eddy simulations. *Geophysical Research Letters*, *42*, 8185–8191. https://doi.org/10.1002/2015GL065140

Geleyn, J., & Hollingsworth, A. (1979). An economical analytical method for the computation of the interaction between scattering and line absorption of radiation. *Beitraege zur Physik der Atmosphaere*, *52*, 1–16.

Hogan, R. J., & Illingworth, A. J. (2000). Deriving cloud overlap statistics from radar. *Quarterly Journal of the Royal Meteorological Society*, *126*(569), 2903–2909.

Jakob, C., & Klein, S. (1999). The role of vertically varying cloud fraction in the parametrization of microphysical processes in the ECMWF model. *Quarterly Journal of the Royal Meteorological Society*, *125*(555), 941–966.

Jakob, C., & Klein, S. (2000). A parametrization of the effects of cloud and precipitation overlap for use in general-circulation models. *Quarterly Journal of the Royal Meteorological Society*, *126*(568), 2525–2544.

Li, J. (2000). Accounting for overlap of fractional cloud in infrared radiation. *Quarterly Journal of the Royal Meteorological Society*, *126*(570), 3325–3342.

Liang, X.-Z., & Wang, W.-C. (1997). Cloud overlap effects on General Circulation Model climate simulations. *Journal of Geophysical Research*, *102*(D10), 11039–11047.

Lock, A., Brown, A., Bush, M., Martin, G., & Smith, R. (2000). A new boundary layer mixing scheme. Part I: Scheme description and single-column model tests. *Monthly Weather Review*, *128*(9), 3187–3199.

Loeb, N., Wielicki, B., Doelling, D., Smith, G., Keyes, D., Kato, S., . . . Wong, T. (2009). Toward optimal closure of the Earth's top-of-atmosphere radiation budget. *Journal of Climate*, *22*(3), 748–766.

Mace, G. G., & Benson-Troth, S. (2002). Cloud-layer overlap characteristics derived from long-term cloud radar data. *Journal of Climate*, *15*(17), 2505–2515.

Morcrette, J.-J., & Fouquart, Y. (1986). The overlapping of cloud layers in shortwave radiation parameterizations. *Journal of the Atmospheric Sciences*, *43*(4), 321–328.

Morcrette, J.-J., & Jakob, C. (2000). The response of the ecmwf model to changes in the cloud overlap assumption. *Monthly Weather Review*, *128*(6), 1707–1732.

Naud, C. M., Del Genio, A., Mace, G. G., Benson, S., Clothiaux, E. E., & Kollias, P. (2008). Impact of dynamics and atmospheric state on cloud vertical overlap. *Journal of Climate*, *21*(8), 1758–1770.

Neggers, R. A., Heus, T., & Siebesma, A. P. (2011). Overlap statistics of cumuliform boundary-layer cloud fields in large-eddy simulations. *Journal of Geophysical Research*, *116*, D21202. https://doi.org/10.1029/2011JD015650

Neu, J., & Prather, M. (2012). Toward a more physical representation of precipitation scavenging in global chemistry models: Cloud overlap and ice physics and their impact on tropospheric ozone. *Atmospheric Chemistry and Physics*, *12*(7), 3289–3310.

Oreopoulos, L., & Khairoutdinov, M. (2003). Overlap properties of clouds generated by a cloud-resolving model. *Journal of Geophysical Research*, *108*(D15), 4479. https://doi.org/10.1029/2002JD003329

Oreopoulos, L., & Norris, P. (2011). An analysis of cloud overlap at a midlatitude atmospheric observation facility. *Atmospheric Chemistry and Physics*, *11*(12), 5557–5567.

Park, S. (2014a). A unified convection scheme (UNICON). Part I: Formulation. *Journal of the Atmospheric Sciences*, *71*(11), 3902–3930.

Park, S. (2014b). A unified convection scheme (UNICON). Part II: Simulation. *Journal of the Atmospheric Sciences*, *71*(11), 3931–3973.

Park, S., Baek, E.-H., Kim, B.-M., & Kim, S.-J. (2017). Impact of detrained cumulus on climate simulated by the Community Atmosphere Model version 5 with a unified convection scheme. *Journal of Advances in Modeling Earth System*, *9*, 1399–1411. https://doi.org/10.1002/2016MS000877

Park, S., & Bretherton, C. S. (2009). The University of Washington shallow convection and moist turbulence schemes and their impact on climate simulations with the Community Atmosphere Model. *Journal of Climate*, *22*(12), 3449–3469.

Park, S., Bretherton, C. S., & Rasch, P. J. (2014). Integrating cloud processes in the community atmosphere model, version 5. *Journal of Climate*, *27*(18), 6821–6856.

Siebesma, A. P., Soares, P. M., & Teixeira, J. (2007). A combined eddy-diffusivity mass-flux approach for the convective boundary layer. *Journal of the Atmospheric Sciences*, *64*(4), 1230–1248.

Stephens, G. L., Li, J., Wild, M., Clayson, C. A., Loeb, N., Kato, S., . . . Andrews, T. (2012). An update on earth's energy balance in light of the latest global observations. *Nature Geoscience*, *5*, 691–696.

Stubenrauch, C., Del Genio, A., & Rossow, W. (1997). Implementation of subgrid cloud vertical structure inside a GCM and its effect on the radiation budget. *Journal of Climate*, *10*(2), 273–287.

Tian, L., & Curry, J. A. (1989). Cloud overlap statistics. *Journal of Geophysical Research*, *94*(D7), 9925–9935.

Willén, U., Crewell, S., Baltink, H. K., & Sievers, O. (2005). Assessing model predicted vertical cloud structure and cloud overlap with radar and lidar ceilometer observations for the baltex bridge campaign of cliwa-net. *Atmospheric Research*, *75*(3), 227–255.

Xie, P., & Arkin, P. (1996). Analyses of global monthly precipitation using gauge observations, satellite estimates, and numerical model predictions. *Journal of Climate*, *9*(4), 840–858.